Topographic Response to Simulated M_w 6.5–7.0 Earthquakes on the Seattle Fault

Ian Stone*[1], Erin A. Wirth[1], and Arthur D. Frankel[1]

ABSTRACT

We explore the response of ground motions to topography during large crustal fault earthquakes by simulating several magnitude 6.5–7.0 rupture scenarios on the Seattle fault, Washington State. Kinematic simulations are run using a 3D spectral element code and a detailed seismic velocity model for the Puget Sound region. This model includes realistic surface topography and a near-surface low-velocity layer; a mesh spacing of ~30 m at the surface allows modeling of ground motions up to 3 Hz. We simulate 20 earthquake scenarios using different slip distributions and hypocenter locations on a planar fault surface. Results indicate that average ground motions in simulations with and without topography are similar. However, shaking amplification is common at topographic highs, and more than a quarter of all sites experience short-period (≤ 2 s) ground-motion amplification greater than 25%–35%, compared with models without topography. Comparisons of peak ground velocity at the top and bottom of topographic features demonstrate that amplification is sensitive to period, with the greatest amplifications typically manifesting near a topographic feature's estimated resonance frequency and along azimuths perpendicular to its primary axis of elongation. However, interevent variability in topographic response can be significant, particularly at shorter periods (<1 s). We do not observe a clear relationship between source centroid-to-site azimuths and the strength of topographic amplification. Overall, our results suggest that although topographic resonance does influence the average ground motions, other processes (e.g., localized focusing and scattering) also play a significant role in determining topographic response. However, the amount of consistent, significant amplification due to topography suggests that topographic effects should likely be considered in some capacity during seismic hazard studies.

KEY POINTS

- We model shaking from M_w 6.5+ earthquakes to characterize topographic effects during finite-fault rupture.
- Modeled topographic effects mirror real-world observations, though variability in response is often large.
- Adding topography to waveform simulations can affect modeled ground motions and may influence hazard analysis.

Supplemental Material

INTRODUCTION

Local site effects are one of the primary controls on the character of earthquake ground motions. Near-surface geology, sedimentary basin structure, and topography all affect seismic wave propagation and can significantly increase the strength of earthquake shaking in certain scenarios. Among these, the contributions of topography are likely the least well understood. Though often coincidental, records of topographic effects on earthquake shaking do exist for a range of different topographic morphologies and earthquake magnitudes (e.g., Davis and West, 1973; Celebi, 1987; Hartzell *et al.*, 1994, 2014; Pedersen *et al.*, 1994; Spudich *et al.*, 1996; Hough *et al.*, 2010; Pischiutta *et al.*, 2010). In many of these cases, topographic effects were invoked to explain conspicuous, localized earthquake damage, typically occurring at the top of hills, ridges, and cliffs. Numerical simulations have helped augment the observational record (e.g., Boore, 1972; Bard, 1982; Sánchez-Sesma *et al.*, 1982; Bouchon *et al.*, 1996), providing a means to model the full wavefield response to topography, whereas analytic relations have allowed us to precisely constrain the factors governing some aspects of topographic response (e.g., Paolucci, 2002).

1. U.S. Geological Survey, Earthquake Science Center, Seattle, Washington, U.S.A., https://orcid.org/0000-0003-2622-2691 (IS); https://orcid.org/0000-0002-8592-4442 (EAW); https://orcid.org/0000-0001-9119-6106 (ADF)

*Corresponding author: istone@usgs.gov

Cite this article as Stone, I., E. A. Wirth, and A. D. Frankel (2022). Topographic Response to Simulated M_w 6.5–7.0 Earthquakes on the Seattle Fault, *Bull. Seismol. Soc. Am.* **112**, 1436–1462, doi: 10.1785/0120210269

Together, these previous studies have demonstrated that topographic effects have a generally consistent set of characteristics:

- Topography has a much larger amplification effect on the horizontal components of ground motion than on the vertical component, which generally manifests as greater amplification in *S*- and surface waves than in *P* waves.
- Topographic highs (e.g., hilltops, ridges, and cliffs) tend to focus and trap seismic energy, resulting in an increase in ground shaking; conversely, topographic lows (e.g., the foot of hills and cliffs or valley bottoms) tend to diffract seismic waves, resulting in a decrease in shaking.
- The magnitude of amplification is both frequency and azimuth dependent. Hills and ridges have the greatest amplification effect on waves with wavelengths approximately equal to their basal width (Boore, 1972). This amplification effect, often referred to as topographic resonance, reduces rapidly as the wavelength increases relative to the basal width; for shorter wavelengths, complex, alternating patterns of amplification and deamplification may manifest along the slopes and near the base of the topography. If the topographic feature has a primary axis of elongation, amplification will be the greatest for waves polarized perpendicular to this axis.
- A topographic feature's height will also influence the response, with amplification increasing with the ratio of height over basal width (Sánchez-Sesma, 1990).

Numerical simulations demonstrate that topography may also significantly scatter the seismic wavefield. Simulations of hills and ridges show that a portion of an amplified *S* wave is converted to *P* and Rayleigh waves, which emanate radially from the topographic feature (Bard, 1982; Bouchon *et al.*, 1996). Similarly, Rayleigh waves interacting with cliff-like features experience increasing deflection when the ratio of cliff height over wavelength is greater than about 0.3 (Martel *et al.*, 1977). Though there are some disagreements between experimentally observed and simulated amplification values, topography may more than double the strength of ground motion at its crest relative to its foot, with some observations noting amplification factors greater than 30 at certain frequencies (Geli *et al.*, 1988).

Despite the influence topography may have on earthquake shaking, topographic effects are seldom considered in seismic hazard analyses, largely because of how difficult they are to accurately constrain. Because topographic effects depend on the azimuth of the incoming wavefield relative to the feature, their impact on ground motions are highly dependent on the location of potential earthquake sources. Compounding this issue is that topography seldom assumes a simple, archetypal form. Many topographic features have complicated morphologies or are composed of a combination of features with varying scale, each of which has its own unique response. Shallow soil layers and local geology, which influence topographic shape, respond in complex ways to ground motions as well. As a result, it may be difficult, if not impossible, to separate the unique contributions of topography to ground-motion amplification (Geli *et al.*, 1988).

In the context of ground-motion simulations, scale presents a significant challenge to accurately modeling topographic amplification. Topographic features that can alter ground motions are often only tens-to-hundreds of meters in width and may only affect shaking at higher frequencies (>1 Hz). Variability in this frequency range due to shallow velocity structure and source distribution is already high, complicating the prediction of topographic response. The computational requirements may also be prohibitively expensive to attempt direct simulations in these frequency ranges over large areas.

However, with the growing availability of high-performance computing, the development of codes capable of handling complex topographies and more near-surface velocity data available at regional scales, it is becoming easier to directly model ground-motion amplification due to topography. At the time of writing, few studies have attempted to simulate the effects of small-wavelength topographic features (<100 m) on ground motions at regional scales (Lee *et al.*, 2008, 2009; Rodgers *et al.*, 2010; Imperatori and Mai, 2015). Such simulations have been useful for constraining the fundamental ways in which topographic effects manifest in realistic earth models. However, extending these results to estimates of ground motion from higher magnitude earthquakes (M_w >5.5) is difficult, as slip can no longer be represented using a point source. The source dimensions for large-magnitude earthquakes may extend into the hundreds of kilometers; the location of the hypocenter within that source area is largely impossible to predict, leading to ambiguity in how effects like directivity may manifest during a given earthquake. Further, slip on the fault surface is spatially heterogeneous, leading to a variable distribution of higher frequency shaking. Simulating the effects of these factors and the variability they introduce to estimated ground motions is a difficult task in and of itself, even without considering the contribution of topographic effects. However, as some seismic hazard characterization methods move toward incorporating direct ground-motion simulations, it is critical to quantify the differences in the ground motions predicted by simulations with and without topography, and how topographic effects are impacted by kinematic rupture parameters.

In this study, we explore the effects of topography on simulated ground shaking from large-magnitude (M_w 6.5–7.0) crustal fault earthquakes. Earthquakes are simulated using a kinematic source model, providing a means to interrogate the sensitivity of topographic response to slip distribution and hypocenter location in finite-fault rupture. A realistic, 3D velocity model allows us to accurately represent wave propagation within our study region, whereas a model mesh with ~30 m surface spacing allows us to resolve ground shaking up to 3 Hz. Besides comparing the response between topography and nontopography simulations, we additionally

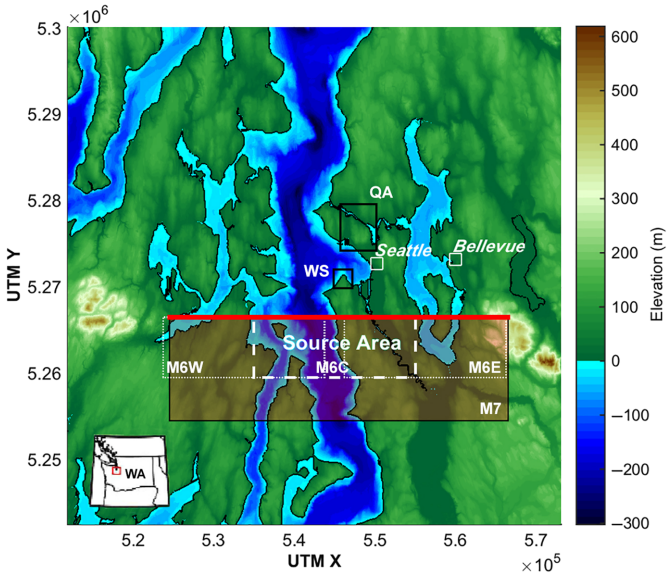

Figure 1. Map of model extent with 30 m sampled topography and bathymetry. Shaded area denotes the surface projection of the M_w 7.0 earthquake source, with the solid red line demarcating the up-dip edge of the rupture plane. The bounds of the central M_w 6.5 source region (M6C) are denoted by the dashed lines, whereas the east and west M_w 6.5 source regions (M6E and M6W) are denoted by dotted lines. Black boxes correspond to West Seattle (WS) and Queen Anne (QA). The inset shows the location of the study area (red box) within the state of Washington. UTM, Universal Transverse Mercator. The color version of this figure is available only in the electronic edition.

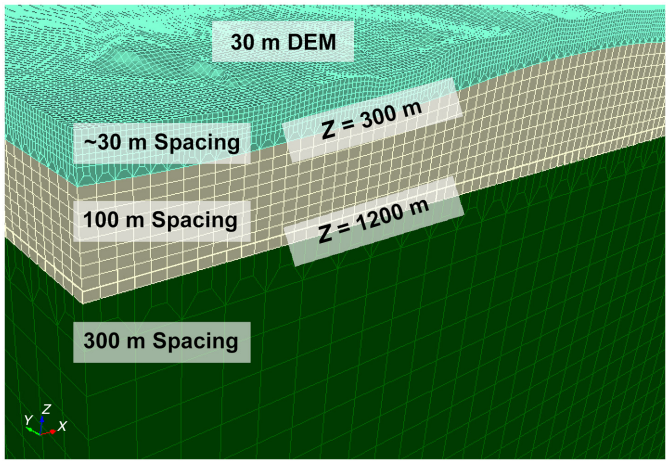

Figure 2. An example of the model mesh used in the spectral element method simulations. The top surface of the mesh is constrained with a 30 m topography digital elevation model (DEM); the full extent of this topographic surface is shown in Figure 1. Spacing of the mesh increases from ~30 m near the surface to 300 m at depths below 1200 m. The color version of this figure is available only in the electronic edition.

compare the simulated peak ground motions with those predicted by the ground-motion models (GMMs) of the Pacific Earthquake Engineering Research Center Next Generation Attenuation-West2 Project (NGA-West2). By examining simulated ground motions from different locations on topographic features throughout the model region in both the time and frequency domains, we are able to broadly characterize simulated topographic effects on earthquake ground shaking.

MODELS AND SIMULATION APPROACH

Regional setting

The region covered in our simulations encompasses the expected source area for an M_w ~7 Seattle fault earthquake, as well as the city of Seattle and much of its metropolitan area (Fig. 1). Topography in the Puget Sound region is largely characterized by glacial geomorphology, as the entire area was buried beneath the Puget lobe of the Cordilleran ice sheet during the last glacial maximum. The principal topographic feature in the model area—the ~250 m deep Puget Sound—is the largest of a series of north–south-trending channels excavated by ice and glacial outwash. Between these channels are drumlins reaching heights of up to ~150 m. Though fairly flat at their crests, the drumlins are flanked by steep slopes and cliffs that drop rapidly down into the channels. The regional topography is also strongly influenced by the Seattle fault—a south-dipping reverse fault that bisects the model area along an east–west surface trace. Rigid sedimentary rocks and crystalline basement are brought to the surface just south of the fault, producing a line of geologically resistant hills; the tallest of these features is the 618 m tall Squak Mountain, which sits near the eastern edge of the model.

SPECFEM3D simulations and model mesh

For kinematic earthquake simulations, we use SPECFEM3D—a spectral element method (SEM) code that adeptly handles complex topographic surfaces and performs well in large, parallel-computing applications (Komatitsch *et al.*, 2004). SPECFEM3D discretizes the wavefield using a mesh of model elements, upon which a realistic velocity model and topographic surface may be imposed. A unique component of the SEM is the use of Lagrange polynomials as basis functions, as well as Gauss–Lobatto–Legendre (GLL) collocation points for interpolation within each element (Fichtner, 2011). A section of mesh used in this study is shown in Figure 2. To maintain an optimal sampling of the velocity structure, the element size was reduced closer to the surface where the lowest velocity materials are located. The average element size in our simulations was reduced from 300 m at depths greater than 1200 m to 100 m from 300 to 1200 m depths, and ~30 m at depths less than 300 m. The ~30 m element size at the surface was selected to honor the dominant scale of regional topography, because the majority of local features have base-to-crest heights of around 100 m and widths greater than 500 m. With five GLL points between each element vertex, average spacing of GLL points at the surface was ~7.5 m.

The topography used to develop the model mesh was primarily taken from a combined topography and bathymetry

TABLE 1
Summary of Topography and Flat Simulation Parameters

Minimum *S*-wave velocity (m/s)	450
Maximum frequency modeled (Hz)	3.0
XYZ Model dimensions (km)	61.2 × 57.6 × 28.8
Elements	29,048,832
Processors required	2,048
Node hours per run (topography vs. flat)	1,344/889
Wall-clock hours per run (topography vs. flat)	42/28
Simulation duration (s)	35
Δt (s) (topography vs. flat)	$4.0 \times 10^{-4}/5.5 \times 10^{-4}$
Total timesteps (topography vs. flat)	87,500/63,700

digital elevation model (DEM) for the Puget Sound, downsampled to 30 m (Finlayson, 2005). Additional elevation data for the eastern portion of the model was taken from the U.S. Geological Survey (USGS) 1/3rd arc-second DEM (USGS, 2017). To reduce mesh distortion and improve simulation stability, a smoothed version of the topography was used to define the refinement boundary at 300 m depth in the mesh. Some locations on the topographic free surface required smoothing to improve model stability. This process is discussed in the supplemental material.

For each rupture scenario, a simulation was run on two different versions of the model mesh: one with topography and one without topography (we will refer to these as "topography" and "flat" simulations throughout the article). This allowed us to directly compare differences in the wavefield due to the topographic surface. Simulations were run on the Stampede2 supercomputer at the Texas Advanced Computing Center. A summary of simulation parameters is included in Table 1.

Seismic velocity model

The seismic velocity model employed in our simulations is a modified version of the Cascadia Velocity Model (CVM) of Stephenson *et al.* (2017). This model reproduces the 3D velocity structure of the region, explicitly incorporating the geometry of Quaternary and Tertiary basin sediments, as well as the Seattle fault. Velocity values in the Puget Sound region are primarily from the active source *P* wave tomography results of Ramachandran *et al.* (2006). For our simulations, we augmented the velocity model with frequency-independent attenuation values as well as a surficial (upper 50 m) low-velocity layer, calculated following the methods outlined in Frankel *et al.* (2018). This surface layer varies velocity according to a randomized field with a standard deviation of 5% and with a characteristic length spanning several kilometers. Inclusion of such a layer improves ground-motion estimates by mimicking the small-scale velocity variations that scatter surface waves and reduce focusing of seismic energy (Hartzell *et al.*, 2010). Water was not included as a part of the velocity model. Nontopography versions of this velocity model were found to accurately represent wave propagation from regional earthquake events (e.g., Frankel *et al.*, 2009; Thompson *et al.*, 2020), and have been employed in a variety of simulations (e.g., Allstadt *et al.*, 2013; Frankel *et al.*, 2018; Wirth, Frankel, *et al.*, 2018), as well as seismic hazard analyses (e.g., Frankel *et al.*, 2007). To test the accuracy of the topography velocity model and the simulation method, we also simulated a small (M_w 3.3), well-recorded local earthquake that occurred within the model area. This test found that body wave arrival times and amplitudes were generally well reproduced; more details on this test are included in the supplemental material.

To accurately simulate wave propagation within topographic features, it is critical that the velocity structure respects the shape of the free surface. For both the topography and flat versions of the simulation, we upsampled the upper 500 m of the velocity model from its initial XYZ spacing of $200 \times 200 \times 100$ m^3 to $100 \times 100 \times 50$ m^3 using the nearest-neighbors' interpolation. The low-velocity values at the surface were restricted to just the top layer of this updated model (i.e., the values were only applied in the uppermost 50 m). For the topography version of the velocity model, the velocity values at 100 m depth were stretched upward in areas with positive topography or were stretched downward in areas with negative topography. As such, the low-velocity surface layer maintained a thickness of 50–100 m throughout the model. All adjustments were limited to the upper 500 m of the velocity model (a schematic illustrating this is shown in Fig. 3). To ensure stability of the simulations, we reduced V_P and V_S at several (~100) points in the velocity model; a more detailed discussion of these alterations is included in the supplemental material.

Source model

The source model used in this study was derived following the rupture generator of Frankel *et al.* (2014). To ascribe slip to a fault surface, the method generates a random field of fractal distributions for which the spectral amplitudes are flat up to a characteristic wavenumber (k) and decay as k^{-2} above that value. Correlation distances in the along-strike and down-dip directions, which define the inverse of the corner wavenumber in each dimension, were determined using the magnitude dependency relations of Mai and Beroza (2002). For the M_w 7.0 source, a value of 14.6 km was used for the along-strike dimension, and a value of 6.9 km was used in the down-dip direction; for the M_w 6.5 source, we use an along-strike value of 8.0 km and down-dip value of 4.6 km. We imposed the resulting slip distributions onto a 45°, south-dipping, planar representation of the Seattle fault. This fault surface is in roughly the same position as the Seattle fault's northernmost strand in Blakely *et al.* (2002) and is similarly aligned with the basin-to-basement velocity discontinuity in the CVM. Dimensions of the rupture zone were determined using the empirical scaling relationships of Wells and Coppersmith (1994). For an M_w 7.0 earthquake, along-strike and down-dip extents were set to 43.7 and 18.2 km, respectively; for

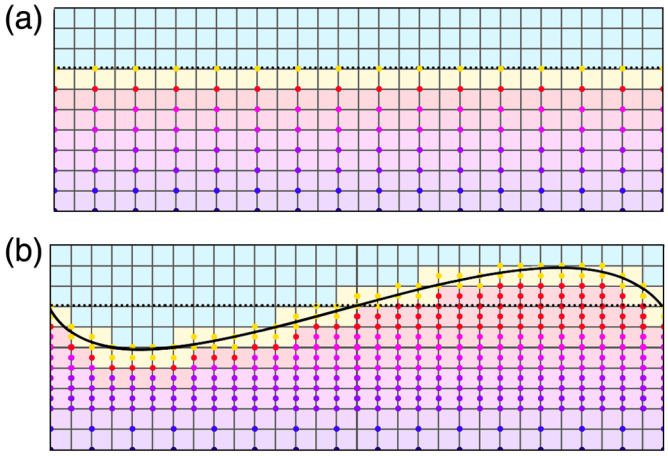

Figure 3. Illustration demonstrating how the velocity model was altered to accommodate topography. The black base grid has a uniform spacing of 100 m, whereas sea level (0 m depth) is represented by a dotted black line. (a) The velocity model before adding topography. Velocity values (colored dots) were spaced every 200 m horizontally and 100 m vertically. The low-velocity layer at 0 m depth is represented by yellow dots, whereas the velocity at 100 m depth is represented by red dots. No velocity values exist for depths above sea level. (b) The velocity model after adding the topographic surface (solid curved line). Spacing was decreased to 100 m horizontally and 50 m vertically. The velocity values at 100 m depth were either stretched upward to meet topographic highs or downward to accommodate topographic lows. The low-velocity surface layer was kept at a near-uniform thickness of around 50 m across the model. The velocity model below 500 m depth was left unaltered. The color version of this figure is available only in the electronic edition.

an M_w 6.5 earthquake, these values were set to 22.4 and 11.4 km, respectively. The upper edge of the fault was located at a depth of 3 km. The horizontal extent of the fault planes is shown in Figure 1.

The slip distribution was decomposed into individual subsources with a uniform spacing of 1 km. Rise time for each subsource was determined by dividing the amount of slip by the slip velocity at the subsource's location. The average slip velocity for all simulations was set to 1.0 m/s—a value consistent with the empirical relationships of Somerville *et al.* (1999) and which produces a constant dynamic stress drop; an additional random variation of ±20% was applied to the slip velocity to reduce rupture coherence. A minimum rise time of 0.5 s was set for all the subsources.

Rupture velocity across the fault surface was set to an average value of 80% of the local *S* wave velocity. This value was scaled by the amount of slip at a given point, such that areas with greater than average slip had faster rupture velocities, and areas with lower than average slip had slower rupture velocities. However, rupture velocity was never allowed to exceed the local *S* wave velocity. Rupture propagation across the fault surface and the subsequent rupture initiation time at each subsource was calculated using 2D ray tracing. Subsource rupture initiation times were then randomly perturbed by a fraction of a second (<0.6 s) to mimic the small-scale variation expected in rupture during actual earthquakes.

Slip was prescribed to each subsource using a moment tensor representative of reverse faulting on the specified fault plane. Rake was randomly varied at each subsource by ±20%. The source time function was represented using a Brune pulse (Brune, 1970). To avoid unrealistic jumps in slip at the edges of the fault, we tapered the slip to zero over the outermost 3 km of the fault.

Variation of rupture parameters and source locations

To judge the sensitivity of topographic effects to variations in rupture parameters, we modeled nine different slip scenarios for both the M_w 7.0 and 6.5 earthquakes. These were defined using three different slip distributions and three hypocenter locations (east, central, and west). The slip distributions and hypocenter locations used for the M_w 7.0 earthquakes are shown in Figure 4. Each slip distribution was created by supplying a new random seed value to the slip generator. Henceforth, we will refer to individual M_w 7.0 slip distribution and hypocenter combinations according to the labels in Table 2.

For the M_w 6.5 earthquakes, in addition to nine combinations of different hypocenter locations and slip distributions, we modeled two source distributions shifted approximately ½ source length to the east and west of the central source location, as shown in Figure 1. This allowed us to interrogate how changing the source location affects topographic response.

RESULTS AND INTERPRETATION

We explore distinct aspects of the simulation results in the following four sections. We start by comparing the topography and flat simulation results with the predictions of empirical GMMs for an M_w 7.0 earthquake; we then discuss the overall effects of topography on ground motions throughout the model region; we interrogate the response on individual, representative topographic features; and we end by exploring variability of response between the topography and flat simulations, with respect to location on the topography, kinematic fault rupture parameters, and source location.

Comparison with empirical GMMs

To validate the simulated ground motions and determine whether adding topography produces an anomalous response, we compare that the simulated M_w 7.0 earthquake results to the predictions from four of the NGA-West2 GMMs (Abrahamson *et al.*, 2014; Boore *et al.*, 2014; Campbell and Bozorgnia, 2014; Chiou and Youngs, 2014). Ground motions were evaluated for a grid of synthetic seismograms with a uniform, 2 km spacing across the entire model region. For the GMMs, we designated a standard V_{S30} value of 600 m/s, which corresponds to the average CVM surface velocity within the model region; basin depth values were calculated using the 1000 and 2500 m/s depth contour from the CVM.

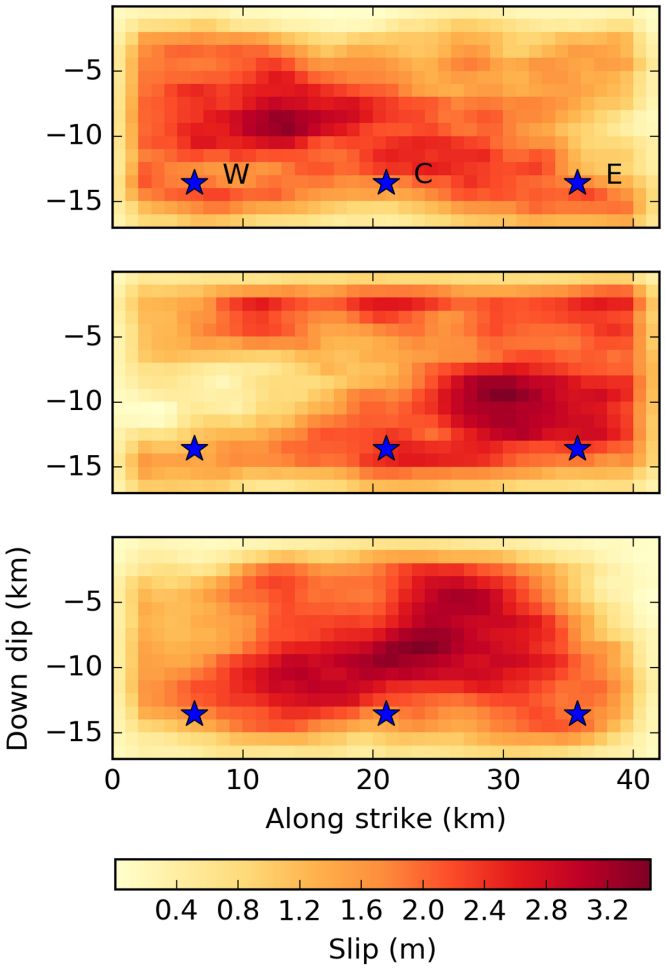

Figure 4. Slip distributions used to define the three different earthquake sources. Stars denote the three different hypocenter locations (C, central; E, east; and W, west). With respect to the scenarios listed in Table 2, slip distributions 1, 2, and 3 correspond to the top, middle, and bottom plots, respectively. The color version of this figure is available only in the electronic edition.

Comparisons of the spectral acceleration (SA) at four response periods (0.3, 1.0, 2.0, and 5.0 s) are shown in Figure 5. For each station in the uniform, 2 km grid, we calculated the median rotated horizontal SA (rotD50, Boore, 2010) and then placed the results into 2 km bins corresponding to the shortest distance to the rupture (R). The mean SA curves represent the average SA within each bin for all the nine earthquake simulations. Curves for the topography and flat versions of the simulation are separated into hanging-wall and footwall components (stations north of the top edge of the rupture were considered to be on the footwall, whereas stations to the south were considered to be on the hanging wall). Also plotted are the within-bin $\pm 1\sigma$ ranges for the footwall component of the topography and flat simulation results. GMM values were estimated along a north–south line running perpendicular to the fault and roughly through the center of the model area. The GMM curve represents the average estimate of all the four GMMs along that line, whereas the shading represents the average total standard deviation.

TABLE 2
Labeling Scheme for the M_w 7.0 Simulation Scenarios

Hypocenter Location	Slip Distribution 1	Slip Distribution 2	Slip Distribution 3
West Hypocenter	S1W	S2W	S3W
Central Hypocenter	S1C	S2C	S3C
East Hypocenter	S1E	S2E	S3E

The topography and flat results tend to produce very similar mean values and standard deviations, with a few exceptions. Near-fault (<10 km) ground motions at 0.3 s are elevated in the topography simulations relative to the flat simulations. This is largely due to short-period resonance signals present in the response on some of the large hills along the periphery of the Seattle basin and on either end of the Seattle fault. These topographies are underlain by higher velocity (>1500 m/s) bedrock in the CVM. As a result, seismic waves reaching the surface in these areas were trapped within the ~50 m thick surficial low-velocity layer, generating resonance patterns. The resulting short-period ground motions in the topography simulations in these areas are often more than twice that in the flat simulations. Similar high-frequency resonance patterns in soft soils overlying high-velocity bedrock have been observed in the region during large earthquakes (e.g., Seward Park, as noted in Frankel *et al.*, 2002). However, the regional thickness of these soil layers is not well constrained, so it is difficult to say whether the distribution and degree of soil resonance effects within the topography simulations are realistic. We avoid these locations when exploring localized high-frequency topographic response later in our analysis. Farther from the fault, the topography is generally underlain by lower velocity basin materials, so the short-period response of the two models converges. Also apparent is a distinct difference in hanging-wall (i.e., south of the fault trace) and footwall (north of the fault trace) response with distance. At near-fault distances, ground motions on the hanging wall are largely similar or slightly higher than on the footwall. However, at longer periods (≥1.0 s), ground motions remain high on the footwall out to large distances, whereas hanging-wall ground motions reduce toward the GMM predictions. Other studies have noted similar behavior in simulation results (e.g., Dreger *et al.*, 2015), which may be a result of strong surface wave generation from up-dip rupture along the dipping fault plane. Footwall ground motions are also influenced by basin effects within the Seattle basin, which has been observed to significantly amplify long-period ground motions during local earthquakes (Frankel *et al.*, 2002, 2009; Thompson *et al.*, 2020; Rekoske *et al.*, 2021). Other studies modeling earthquake ground motions in the basin have found

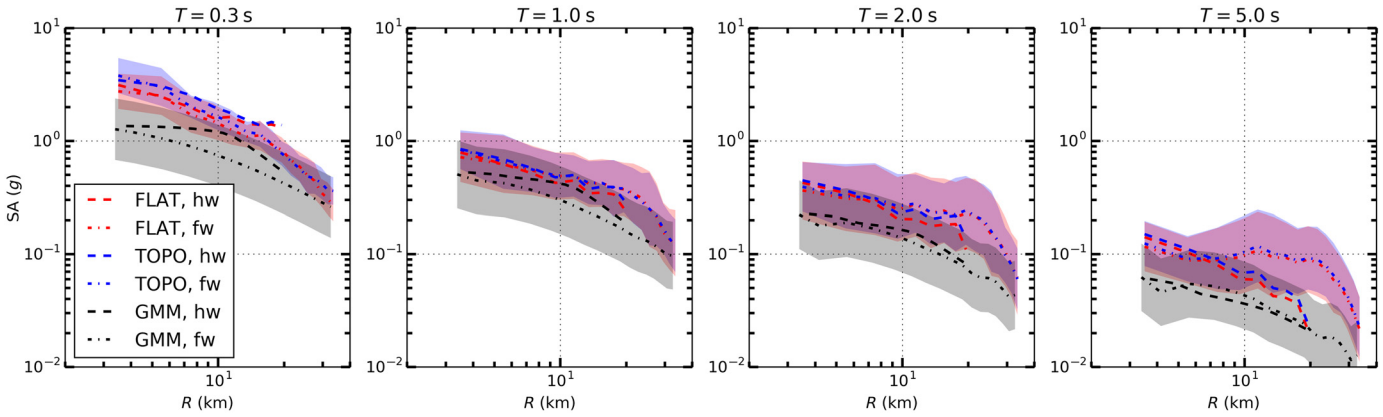

Figure 5. Spectral acceleration (SA) versus the closest distance to the fault (R) at different periods of ground motion, separated into hanging wall (hw) and footwall (fw) curves. Black curves represent the average ground motion from four Next Generation Attenuation-West2 Project ground-motion models (GMMs). Shaded areas represent the $\pm\sigma$ range for the predicted and simulated ground motions (footwall only). TOPO, topography model results; FLAT, flat model results. The color version of this figure is available only in the electronic edition.

that simulated long-period results tend to produce higher values than those estimated by GMMs (Allstadt *et al.*, 2013; Wirth, Chang, *et al.*, 2018).

In aggregate, both topography and flat results tend to estimate higher ground motions than the GMMs for all periods. The GMM standard deviations are large (ranging from around twice as large as the simulation variability at low periods to about the same size at longer periods) and encompass much of the mean simulated ground motions. However, there are some period and distance combinations wherein the simulated ground motions go well beyond the GMM estimates. To directly quantify how much the simulated ground motions deviate from the GMM estimates, we calculate the epsilon value (ε):

$$\varepsilon = \frac{\mu_{\mathrm{Sim}} - \mu_{\mathrm{GMM}}}{\sigma_{\mathrm{GMM}}}, \tag{1}$$

in which μ_{Sim} is the logarithmic mean SA for the simulated results, μ_{GMM} is the logarithmic mean of the GMM estimates, and σ_{GMM} is the logarithmic, mean total standard deviation of the GMM estimates. For this calculation, we evaluated the GMMs at each point within the model region to match the format of the simulation results. We plot ε averaged for all stations versus off-fault distance in Figure 6 and ε mapped across the model region in Figure 7, for several different response periods. Short-period (0.3 s) simulated ground motions are elevated with respect to the GMM estimates at near-fault distances, particularly in the topography model. Again, this is largely due to the effects of the near-surface low-velocity layer, which overlies much higher velocity material near the ends of the fault and which produces resonance signals in some simulations. Longer period ground motions tend to assume values in line with the GMM predictions at near-fault distances. However, beyond ~15 km there is a distinct increase in the average ε-value, particularly for periods ≥2.0 s. The distinct "bump" in the 2.0 and

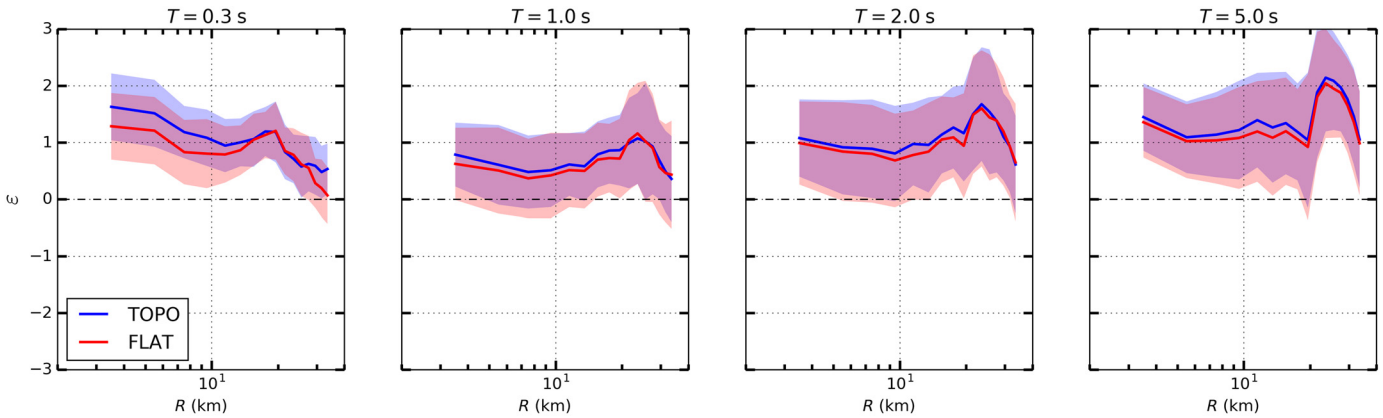

Figure 6. Epsilon (ε) values versus the closest distance to the rupture (R) at different periods of ground motion. Epsilon values are relative to the median of the empirical GMMs. Shaded areas represent the $\pm\sigma$ range for the simulated ground motions. The color version of this figure is available only in the electronic edition.

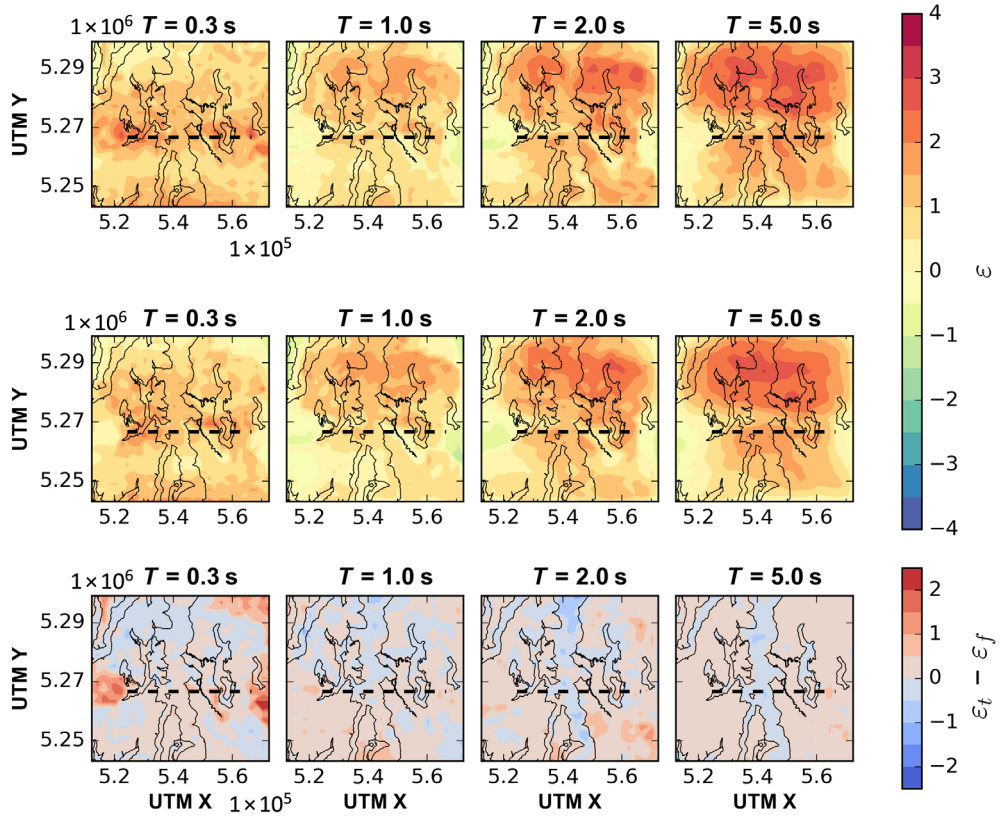

Figure 7. Epsilon (ε) values mapped across the model region at different periods of ground motion. The first and second rows describe the ε-values for the topography and flat simulations, respectively. The third row describes the difference between the topography and flat simulations. The dashed line denotes the surface trace of the fault. The color version of this figure is available only in the electronic edition.

Overall, the ground motions between the topography and flat simulations deviate from GMMs in similar ways. ε anomalies are in the same general locations and are near the same values. This suggests that, in and of itself, adding topography to the simulation generally does not produce ground motions outside the range of empirical estimates. However, it is clear that individual topographic features have some effect on the spatial distribution of ε. This is most apparent in the 5.0 s plot of Figure 7, in which a positive ε anomaly follows the ridgeline of a north–south-trending peninsula near the center of the model region.

Overview of topographic effects on simulated ground motions

To interrogate the overall effects of topography on the M_w 7.0 simulation results throughout the model area, we directly compare the results between the topography and flat models. We compare snapshots of the vertical velocity field as measured at the surface during simulation S2E (Fig. 8). At 5.4 s, shortly after seismic energy has reached the surface, there is little obvious difference in the flat and topography results. However, as time progresses and surface waves propagate northward from the fault, the wavefield is scattered by topographic features. This scattering manifests as a reduction in coherence of the surface wave front, as is apparent starting in the 11.9 s snapshot. By 25.8 s, the coherence of the main surface wave front has significantly degraded in the topography simulation relative to the flat simulation.

In Figure 9, we plot the percentage of peak ground velocity (PGV) amplification in the topography model relative to the flat model (simulation S2E). This percentage is calculated by subtracting the horizontal PGV at every point on the surface in the flat model from the PGV in the topography model, dividing the difference by the PGV in the flat model and then multiplying by 100. PGV throughout the region is dominated by the *S* wave and surface wave components of the response and thus should be sensitive to surface topography. Though there is significant spatial variability in amplification, some general trends are apparent. Topographic highs, such as hill tops and cliffs, typically

5.0 s curves is partially caused by the lack of hanging-wall stations present at larger distances, which allows the footwall estimates to dominate the more-distant response. These footwall ground motions are heavily influenced by basin response at large distances and long periods, which are much higher than the predicted GMM estimates. In addition, forward rupture directivity from the deep hypocenter locations preferentially projects long-period energy into the basin. The GMMs, which span a larger set of scenarios, likely moderate the contribution of such effects.

Another factor contributing to elevated median ground-motion values may be the chosen fault dimensions, which affect the stress drop of the modeled source. Although the Wells and Coppersmith (1994) empirical relations suggest that an M_w 7.0 source should have an area of ~795.3 km^2, empirical relations derived through other methods produce larger source areas. For example, the magnitude–rupture–area relation of Somerville *et al.* (1999) suggests an M_w 7.0 source area of ~1122.0 km^2, which is 40% larger. Confining the moment of an M_w 7.0 earthquake source to a smaller region increases the static stress drop per unit area on the fault surface, which in turn produces higher amplitude ground motions.

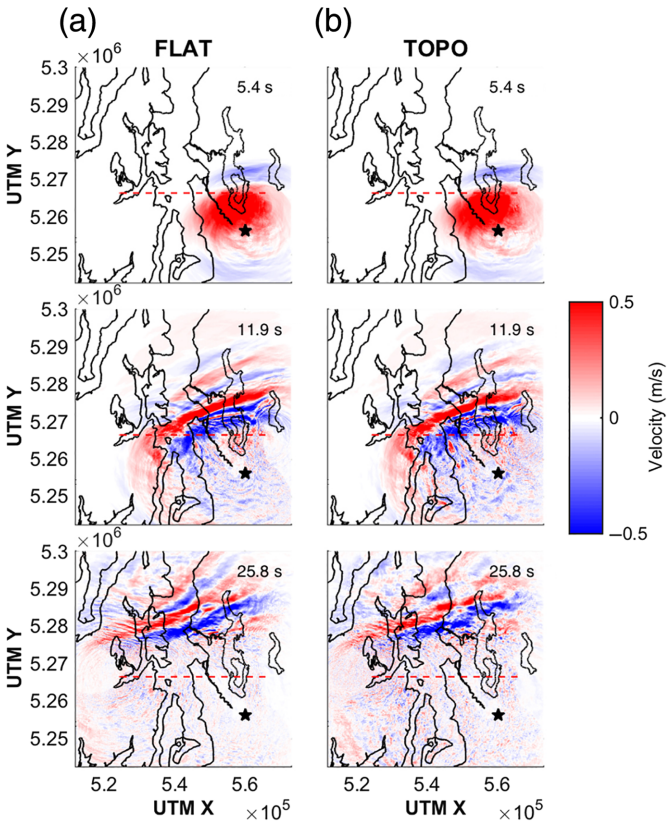

Figure 8. Snapshots of the vertical velocity wavefield at different times for a (a) flat and (b) topography simulation (simulation S2E). Warm colors represent upward velocity, whereas cool colors represent downward velocity. The hypocenter location for this scenario is represented by a star. The color version of this figure is available only in the electronic edition.

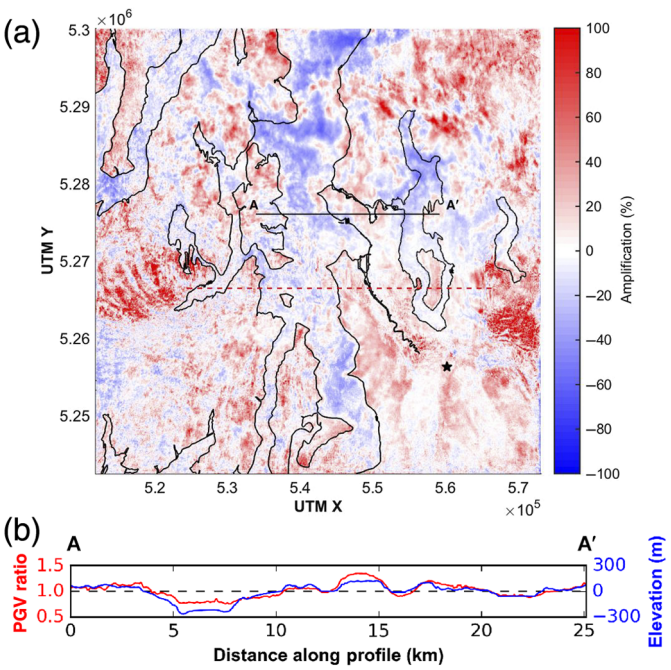

Figure 9. Amplification of the peak ground velocity (PGV) in the topography simulation relative to the flat simulation (simulation S2E). (a) Percentage amplification mapped over the full model extent. Amplification at a particular point on the map is calculated by subtracting the horizontal PGV in the flat model from the PGV in the topography model, dividing by the PGV from the flat model, and then multiplying by 100 to get an amplification percentage. The hypocenter location for this scenario is represented by a star. (b) Horizontal PGV ratio over the profile A–A′ for ground motions at a period of 5 s. The ratio curve (red) represents the average ratio of the root mean square horizontal ground motions from three different simulations (simulations S2W, S2C, and S2E). Also plotted is the elevation along the profile (blue). The color version of this figure is available only in the electronic edition.

experience ground-motion amplification, whereas topographic lows, like valley bottoms and channels, experience deamplification. This trend persists at a variety of scales, occurring both on smaller features (<500 m in width) as well as large features (several kilometers in width). These patterns may overlap with one another, resulting in a superposition of amplification patterns. As noted in the previous section, significant amplification manifests on the mountains on the east and west ends of the fault associated with high-frequency resonance in the low-velocity surface layer. The dependence of peak ground motions on topography is reinforced by the bottom plot in Figure 9, which presents a cross section of topography versus flat horizontal PGV ratios extending from Bainbridge Island to the east bank of Lake Washington (profile A to A′ in the upper plot). The values used to generate this plot represent the average PGV at a period of 5 s between three simulations with different hypocenter locations (simulations S2W, S2C, and S2E). The amplitude of the PGV ratio roughly follows the trend of the large-scale topography; the most negative values are associated with the sunken channels, whereas the most positive values are associated with the elevated isthmus of land between the two channels.

We quantify the generalized distribution of amplification in the topography simulation in Figure 10, in which we plot the aggregate percentage of amplification versus period (Fig. 10a), as well as histograms showing the natural log of the PGV ratio at each period (Fig. 10b). To generate the plots in this figure, we used the PGVs from all the nine simulations recorded on the uniform grid of stations, excluding stations situated in areas directly overlying bedrock (to avoid the combined effects of topography and soil resonance). For all periods of ground motion, a site in the topography simulation will on average record peak ground motions at or slightly above (≤16%) what would be predicted in the flat simulation (Fig. 10a). However, larger amplifications and deamplifications are common. For periods between 0.3 and 2.0 s, half of the observations are amplified or deamplified by more than 25%–35%; about 5% of sites see amplification greater than ~80%. For longer periods (5.0 and 7.5 s), the spread of amplifications is much smaller, with over 90% of sites seeing amplification less than 50%. The logarithm of the topography versus flat PGV ratio indicates

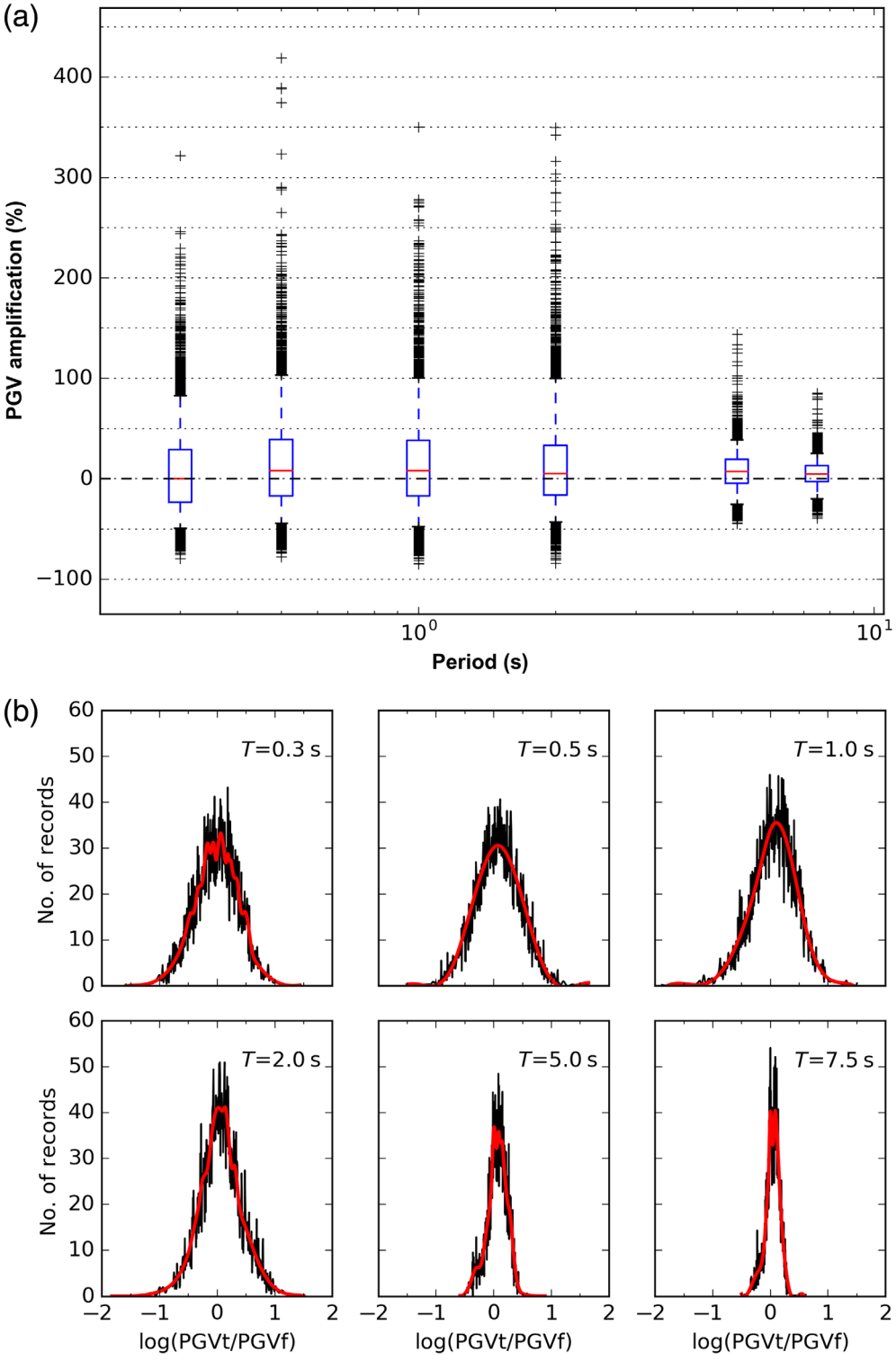

Figure 10. Distributions describing the amplification between the flat and topography simulations across stations in the uniform grid (excluding stations over bedrock). (a) Percentage of amplification, where location along the *x* axis represents the period of ground motion. Each box bounds 50% of observations, with the red line representing the median value of the distribution. Whiskers bound 90% of observations. Black crosses denote observations in the 5th and 95th percentiles. Positive values represent an amplification in ground motion in the topography simulation relative to the flat simulation, whereas negative values represent deamplification. (b) Natural log of the topography versus flat PGV ratio. Each plot shows a histogram of ratio values at each period. The black curve is the raw histogram, which is split into ~640 bins. The red curve is the histogram averaged across 10 bins. PGVf, Peak Ground Velocity flat; PGVt, Peak Ground Velocity topography. The color version of this figure is available only in the electronic edition.

that amplifications due to topography assume a roughly lognormal distribution, the standard deviation of which is greater for periods ≤2 s (Fig. 10b). Consequently, it is more common for ground motions to be amplified than deamplified in the topography model.

Localized effects of topography

The influence of topography on ground shaking is highly dependent on a topographic feature's shape and orientation. To survey the effects of topography in our simulations, we placed synthetic seismogram arrays on a variety of topographic features throughout the model area, spanning a range of sizes, shapes, and orientations. Although the results presented here reflect observations from all of these locations, we focus the bulk of our discussion on two representative features (Fig. 11). The first is West Seattle—a north–south-trending peninsula that tapers to a width of 400–600 m at its northern terminus and which is bounded by 70–110 m tall cliffs. The second feature is Queen Anne—a 142 m tall, oblong drumlin with a width of ~2100 m perpendicular to its major southeast axis. West Seattle is representative of cliff response in the simulations, whereas Queen Anne is representative of hill response. Both of these features sit on the footwall within the Seattle basin and should thus be free from the shallow soil effects seen at some locations outside of the basin. The basin sediments are sufficiently thick at these locations (>1 km) such that seismic velocity is mostly homogenous

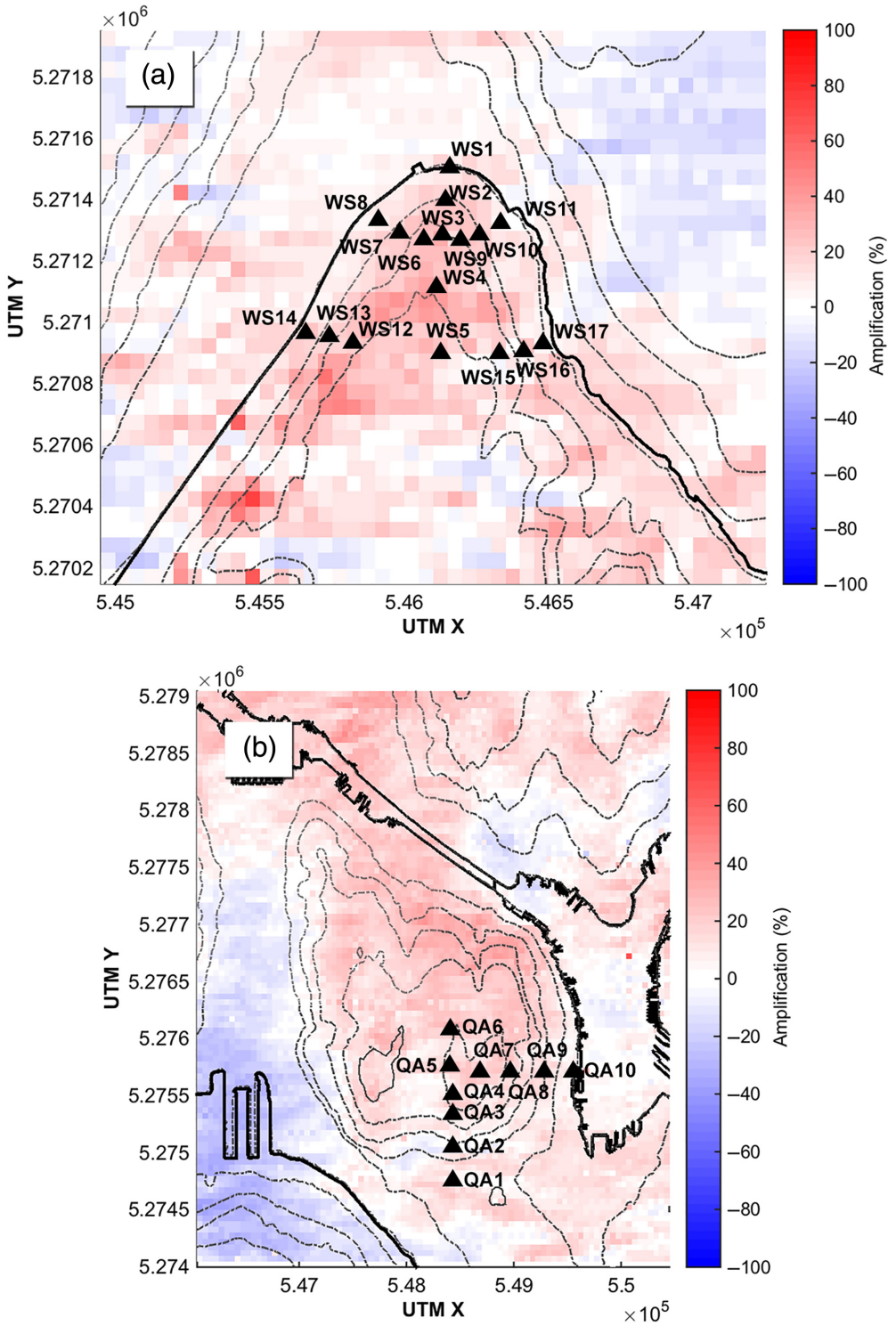

Figure 11. Horizontal PGV amplification in the topography model relative to the flat model on (a) West Seattle and (b) Queen Anne for simulation S2E. Contour interval is 25 m. The locations of West Seattle and Queen Anne within the greater model area are shown in Figure 1. The color version of this figure is available only in the electronic edition.

throughout the topography, and the observed response between the top and bottom of these features is largely attributable to topography, because the shallow basin sediments are similar in velocity to the surface layer.

Time-series observations. Mapping the ratio of the root mean square horizontal PGV at the representative sites for simulation S2E demonstrates that ground shaking is typically amplified at the top of hills and cliffs and less- or deamplified at topographic lows relative to the flat model (Fig. 11). We plot seismograms from the same simulation recorded at the top (WS12), on the slope (WS13), and at the bottom (WS14) of the cliff surrounding West Seattle in Figure 12. *P* wave arrivals see little to no amplification in the topography results relative to the flat results, whereas *S* and surface waves see significant amplification. Station WS12 at the top of the cliff experiences *S* wave and surface wave amplification in all the three components of its response, with a particularly strong amplification in its surface wave around 15 s, in which the velocity in the north direction is nearly doubled between the flat and topography simulations. By comparison, station WS14 at the foot of the cliff does experience some amplification, though less than either of the other stations. The effect of topography on the response at WS13 is more amplified than at WS14 but less amplified than at WS12. At all the three stations, there is a small but systematic delay between the respective phase arrivals in the topography and flat simulations. We attribute this delay to the additional travel time between sea level and the topographic surface.

Frequency-dependent effects. Amplification due to topography is often linked to a characteristic frequency related to the physical dimensions of a topographic feature (Massa *et al.*, 2014). At this "topographic resonance" frequency (f_r),

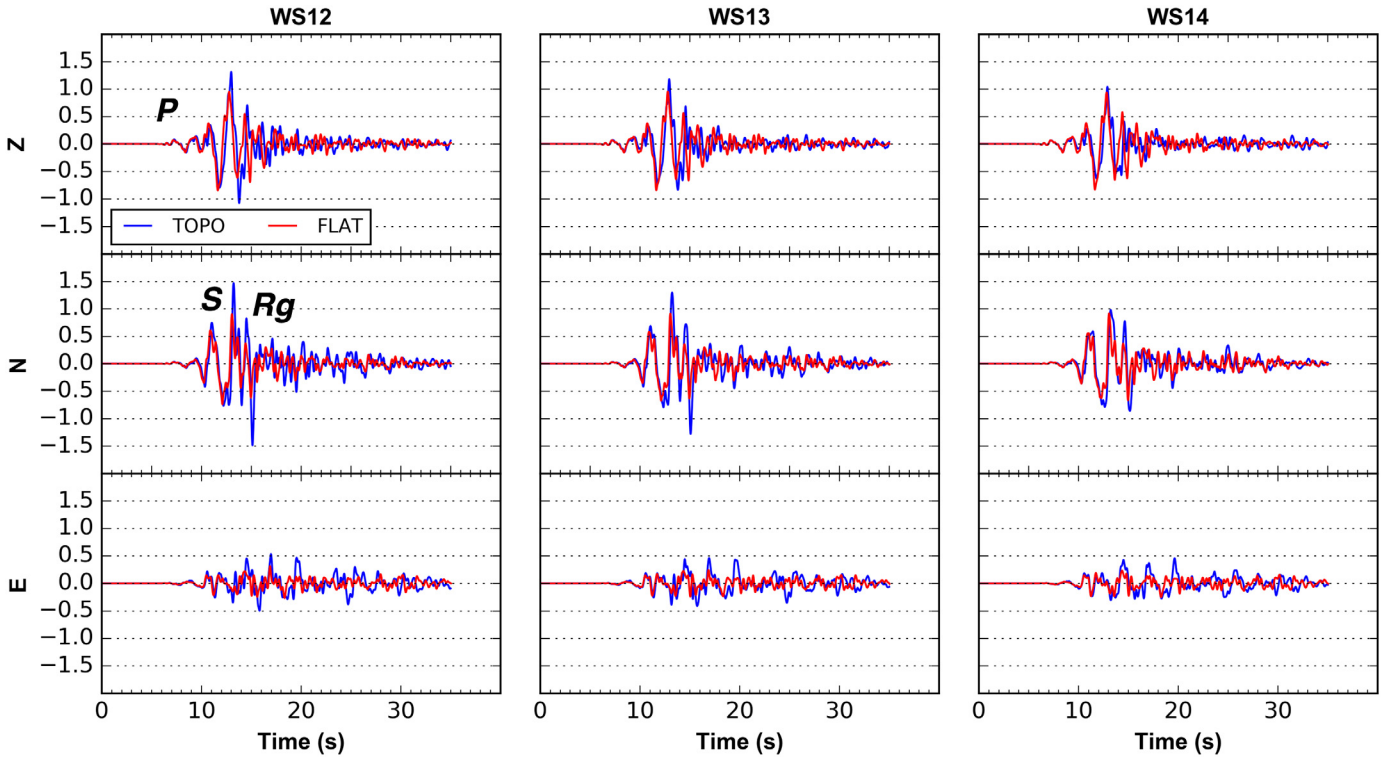

Figure 12. Three-component velocity seismograms recorded on the top (WS12), slope (WS13), and bottom (WS14) of a cliff at West Seattle (simulation S2E). The *P*, *S*, and surface (*Rg*) waves are labeled for station WS12. The color version of this figure is available only in the electronic edition.

ground motions at the top of a feature are significantly amplified relative to surrounding flat ground sites. To judge how much topographic resonance may contribute to the ground-motion amplification observed in our simulations, we compare the response at different frequencies on West Seattle and Queen Anne.

Ashford and Sitar (1997) used numerical simulations of *S* waves interacting with cliffs to derive a relationship for the fundamental frequency of cliff-like features. Based on their observations, they found that ground motions are maximized when seismic waves have a frequency equal to $V_S/5H$, in which V_S is the *S* wave velocity, and H is the height of the cliff. Near-surface velocities in the vicinity of West Seattle are between 500 and 1000 m/s; cliff heights at the northern end of the peninsula are ~75 m tall. Therefore, we expect topographic resonance frequencies around 1.33–2.67 Hz.

Paolucci (2002) derived an analytical relationship between the basal width of a triangular hill or mountain and the feature's resonance frequency. For features with an average *S* wave velocity V_S and width L, the resonance frequency may be predicted using the equation $f_r = C * V_S/L$, in which C is a constant around 0.7–1.0, depending on the height-to-width ratio of the hill and whether *SV* or *SH* waves are under investigation. For Queen Anne, near-surface velocities are also in the 500–1000 m/s range, and the basal width perpendicular to the principle axis is ~2.1 km. Using these values and Paolucci's relation for *SH* waves, we calculate the fundamental frequency of Queen Anne to be around 0.18–0.36 Hz.

We decompose the ratio of the horizontal PGV on West Seattle and Queen Anne into different periods of ground motion (0.3, 0.5, 1.0, 2.0, 5.0, and 7.5 s, respectively) for simulation S2E in Figures 13 and 14. PGV values at each period were calculated by filtering the two horizontal velocity time series at each location on the surface at the period of interest (using a ±0.1 Hz buffer), calculating the root mean square of the two time series and then finding the maximum value. With increasing period, the size of individual amplification and deamplification patches increases, corresponding to the wavelengths of the waves most affected at that period. For the cliffs around West Seattle, we would expect the topography to affect ground motions most in the 0.3–1.0 s range. The greatest evidence for cliff-related amplification occurs in the 0.5 s (i.e., 2.0 Hz) plot (Fig. 13b), in which there is a semidistinct band of amplification and deamplification following the trend of the cliffs, particularly near the northwest end of the peninsula. At the same time, there is little evidence for cliff-related amplification at 0.3 and 1.0 s (3.0 and 1.0 Hz; Fig. 13a,c).

On Queen Anne, we would expect the hill to amplify ground motions most in the 2.0–5.0 s range. There is little evidence for systemic amplification due to topography for periods between 0.3 and 2.0 s (Fig. 14a–d). However, distinct banding patterns are present at 1.0 and 2.0 s. We suggest that these patterns reflect differences in the surface wave field between the

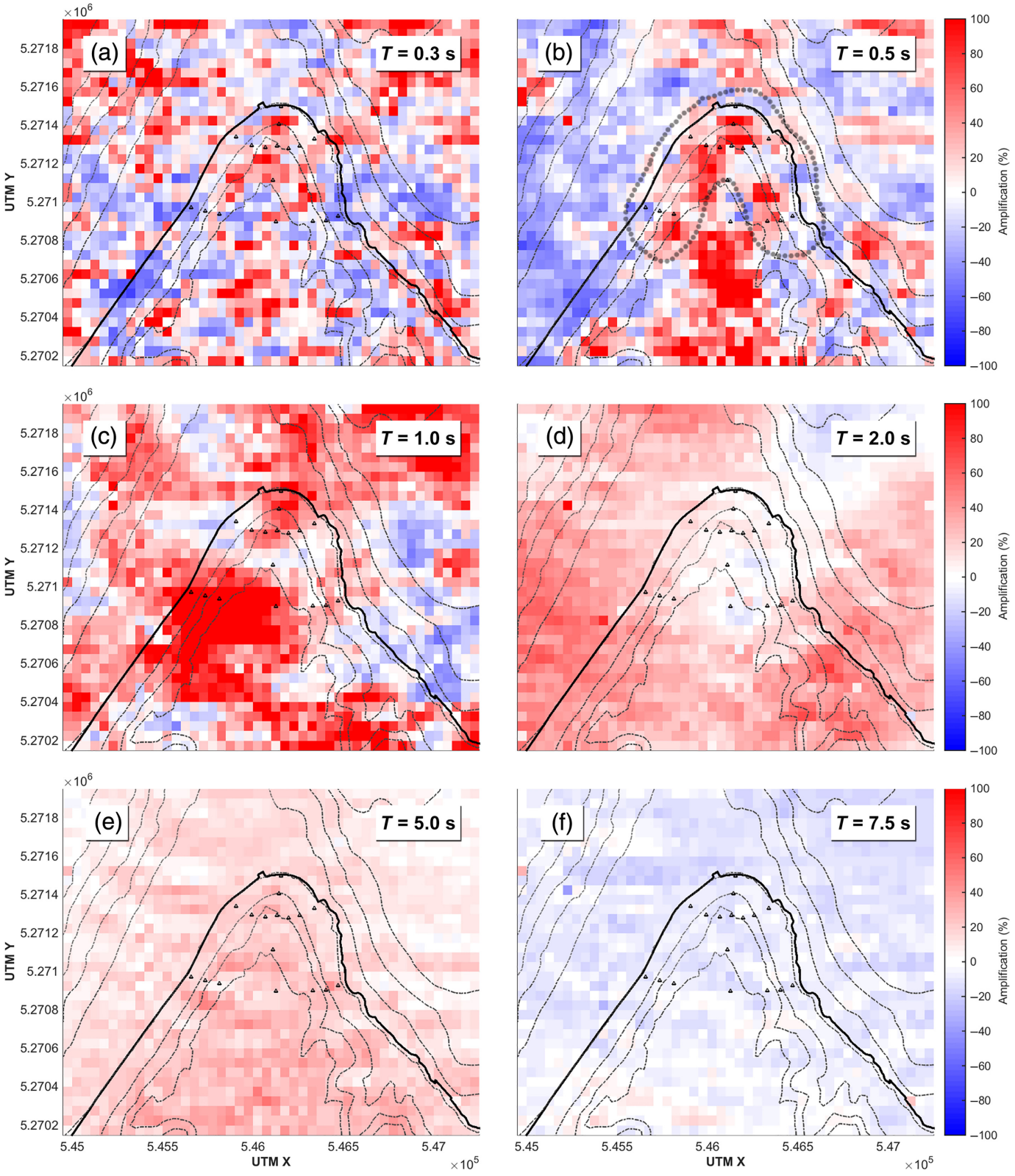

topographic and flat simulations. Surface waves formed at the southern boundary of the Seattle basin are scattered by topography as they propagate northward. The resulting changes in path affect the dispersion pattern of the waves and alter where they reach peak amplitude. Between 5.0 and 7.5 s (0.2 and

Figure 13. Horizontal PGV amplification on West Seattle for simulation S2E at periods of (a) 0.3, (b) 0.5, (c) 1.0, (d) 2.0, (e) 5.0, and (f) 7.5 s. Dotted lines in (b) outline areas of possible amplification and deamplification around the cliffs. The color version of this figure is available only in the electronic edition.

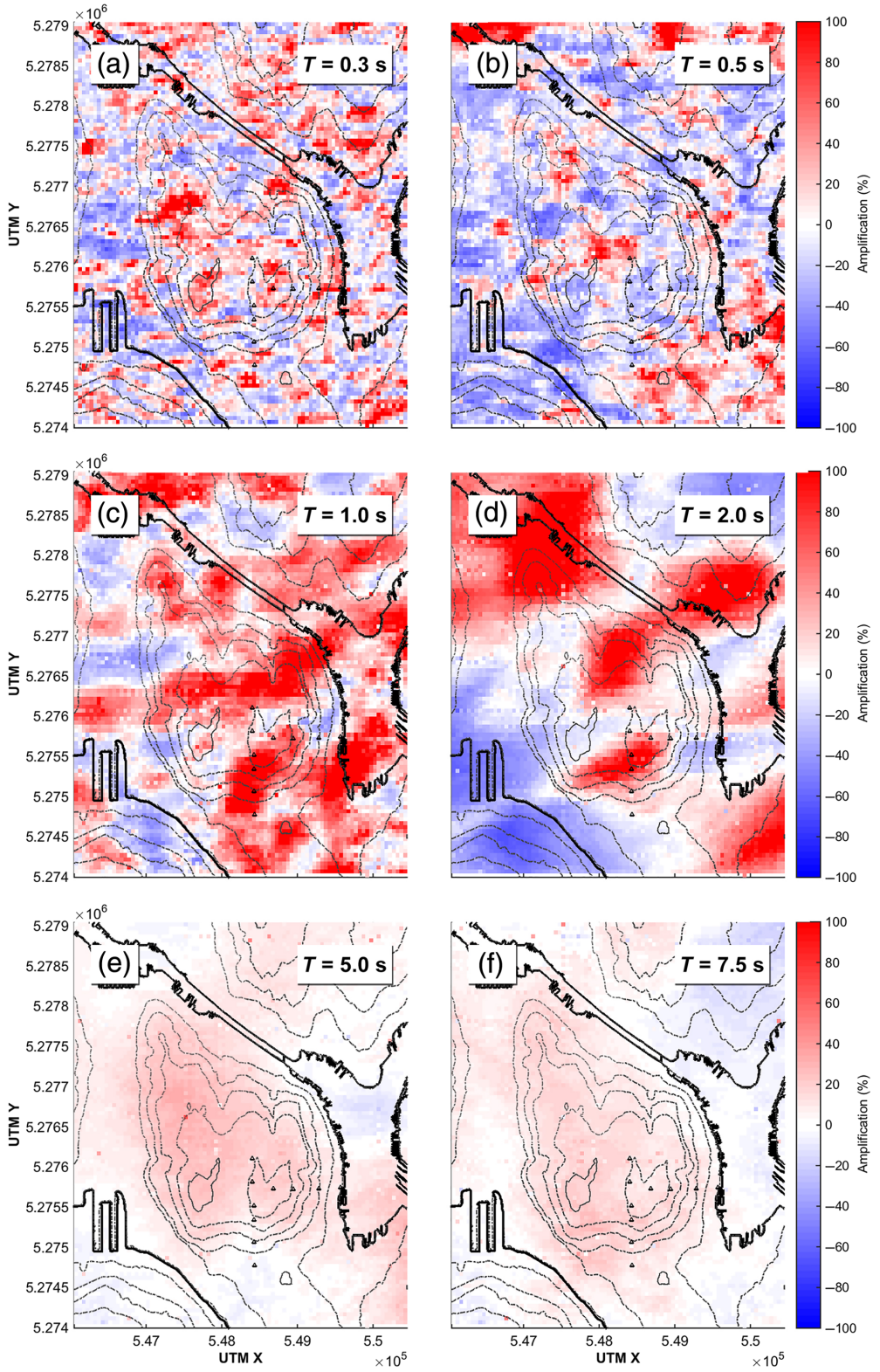

Figure 14. Horizontal PGV amplification on Queen Anne for simulation S2E at periods of (a) 0.3, (b) 0.5, (c) 1.0, (d) 2.0, (e) 5.0, and (f) 7.5 s. The color version of this figure is available only in the electronic edition.

0.13 Hz; Fig. 14e,f), there is evidence for uphill PGV amplification on Queen Anne, with the pattern being the greatest near 5.0 s.

Although useful for illustrating lateral patterns in amplification between the topography and flat simulations, the plots in Figures 13 and 14 do not directly quantify the strength of ground motion at the top of a feature relative to its bottom. When considering the mapped amplification patterns, it is difficult to separate the contribution of local topography from that associated with mid- and far-field scattering of the incoming wavefield. A similar effect was reported in Pitarka *et al.* (2021), in which the authors noted that simulated PGA amplifications in their model region did not correlate well to particular topographic highs, which they attributed to interference from high-frequency waves scattered by the surrounding topography. To isolate the amplification due to a particular topographic feature, we use the targeted arrays of synthetic seismograms, taking the ratio of horizontal PGV between the top (and slope) seismograms over the PGV of the bottom seismogram. This calculation only considers the results of the topography simulation, so we can interrogate the effects of topography independent of the flat results. We plot the amplification at several different periods for simulation S2E at West Seattle in Figure 15. These plots show clear uphill amplification for periods between 0.3 and 1.0 s; there is little to no amplification at periods above 1.0 s. The shorter period amplification pattern is not uniform for all

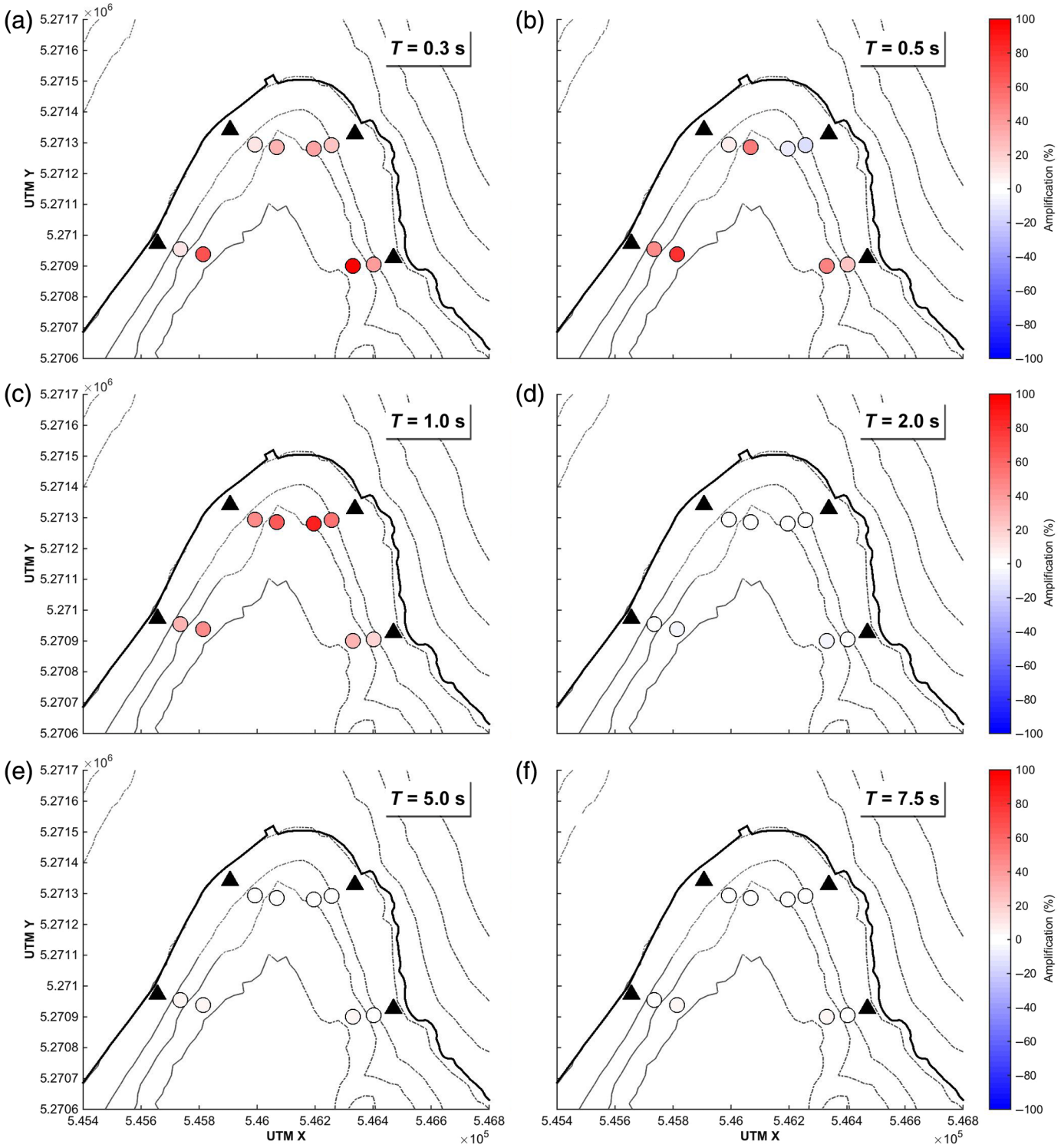

locations (e.g., the northeast set of stations at 0.5 s, Fig. 15b). It is not uncommon to see mixed patterns of amplification at 0.3 and 0.5 s from one simulation to the next (we discuss this variability more in the next section); in contrast, the uphill amplification pattern at 1.0 s persists for all simulations. Based on these observations, we suggest that, within our model setup, the cliffs' topographic resonance lies somewhere between 1.0 and 2.0 Hz, and that there is consistent, predictable amplification near these

Figure 15. Top-over-bottom horizontal PGV amplification at targeted array stations on West Seattle for simulation S2E. Periods of ground motion considered are (a) 0.3, (b) 0.5, (c) 1.0, (d) 2.0, (e) 5.0, and (f) 7.5 s. Top and slope stations are represented by colored circles, whereas the bottom stations are represented by black triangles. The amplification values represent the PGV amplification at the top and slope stations relative to the bottom stations. The color version of this figure is available only in the electronic edition.

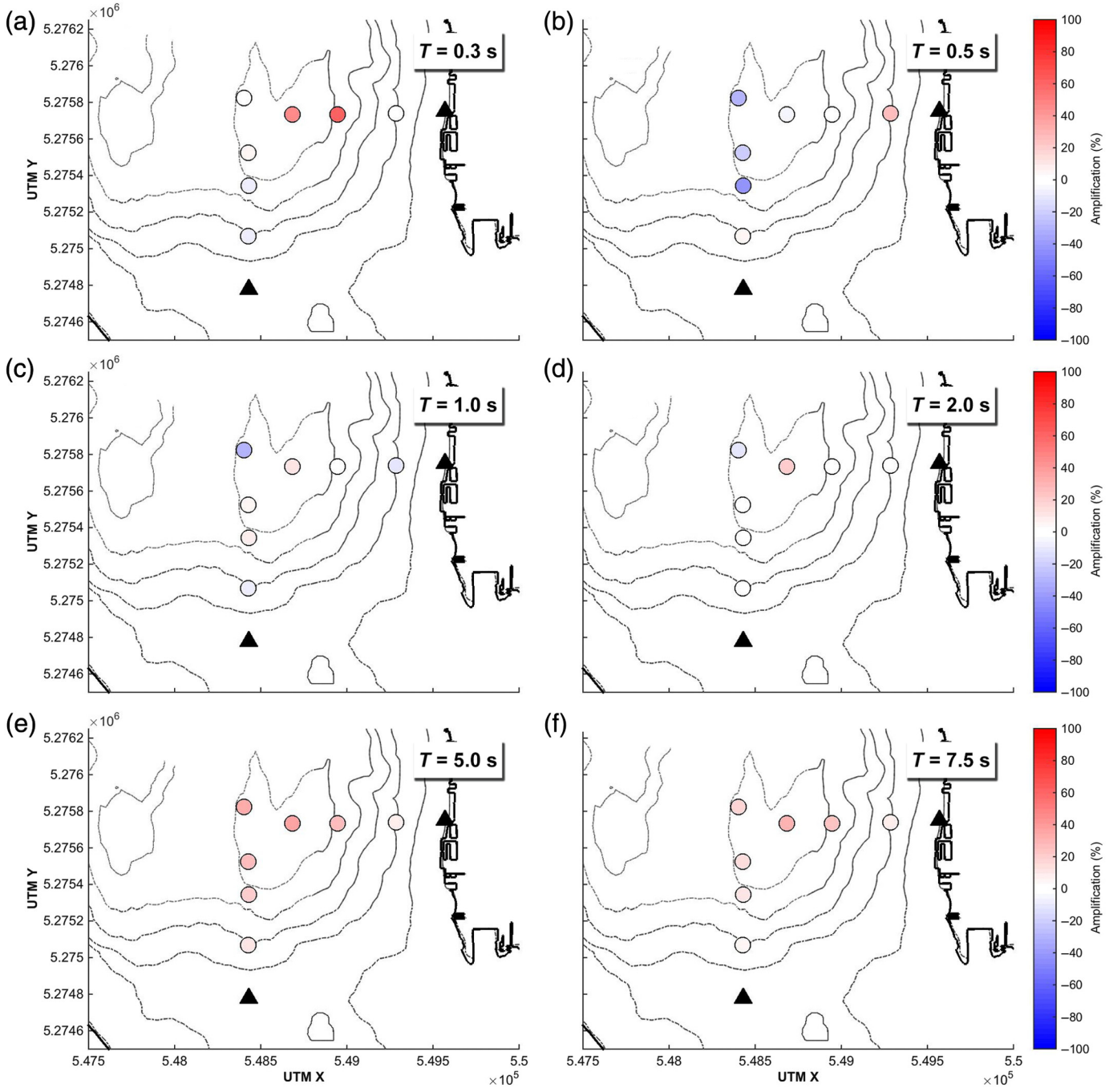

frequencies. Longer periods of seismic wave are not affected by the cliffs, whereas shorter period waves experience complex scattering that varies the amplification pattern from one simulation to the next.

The stations on Queen Anne show little consistent amplification for periods between 0.3 and 2.0 s (Fig. 16a–d). As on West Seattle, whether a station experiences amplification or deamplification changes from one simulation to the next for these shorter periods. Uphill amplification only persists between 5.0 and 7.5 s.

Another characteristic behavior of topographic resonance is its azimuthal dependence. Amplification of ground shaking is

Figure 16. Top-over-bottom horizontal PGV amplification at targeted array stations on Queen Anne for simulation S2E. Periods of ground motion considered are (a) 0.3, (b) 0.5, (c) 1.0, (d) 2.0, (e) 5.0, and (f) 7.5 s. Top and slope stations are represented by colored circles, whereas the bottom stations are represented by black triangles. The amplification values represent the PGV amplification at the top and slope stations relative to the bottom stations. For Queen Anne, QA1 was used as the base station for QA2, QA3, QA4, and QA5, whereas QA10 was used as the base station for QA7, QA8, and QA9. The color version of this figure is available only in the electronic edition.

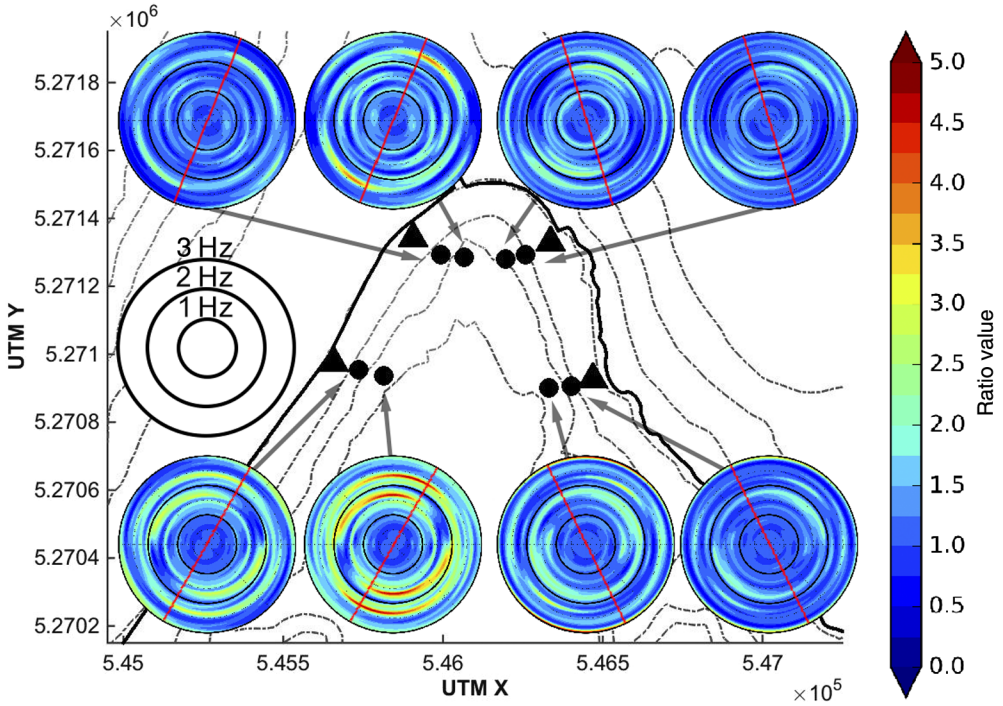

Figure 17. Polarization of horizontal spectral ratios on West Seattle (simulation S2E). Ratios are calculated by dividing the rotated spectral response from stations at the top and slope of the cliff (black circles) by the spectral response at the bottom of the cliff (black triangles). Frequency increases outward from the center of the plot, whereas azimuths correspond to compass directions. Concentric rings mark 1 Hz intervals, with the innermost ring representing 1 Hz and the outermost ring representing 3 Hz. Colors correspond to the value of the spectral ratio at a particular frequency and azimuth. Ratio values greater than one represent amplification relative to the bottom station, whereas values less than one represent deamplification. Red lines denote the approximate primary axis of orientation for the cliff at the point of measurement. The color version of this figure is available only in the electronic edition.

typically the greatest perpendicular to a topographic feature's primary axis of elongation. We explore how amplification changes with azimuth for simulation S2E in Figures 17 and 18. To develop these polarization plots, we rotate the horizontal components of the seismogram at five-degree increments between 0° and 180°, calculating the Fourier spectra at each increment. The spectra are smoothed using a Gaussian function to reduce variability in the response. We then take the ratio of the spectra at the top (and slope) of a feature over the spectra at the bottom of the feature. The resulting plots show the ratio of amplification at a range of frequencies and azimuths.

On West Seattle, there is a distinct dependence of the amplification patterns on the azimuth of the cliffs (Fig. 17). The greatest amplifications (ratio values of ~3–4) are generally at azimuths roughly perpendicular to the primary axis of elongation. However, there are typically multiple "peaks" in amplification along this azimuth, as opposed to a single strong peak at the expected resonance frequency. In reviewing the plots from other simulations, the highest amplification does often fall between 1.0 and 2.0 Hz, though there are occasionally larger peaks at higher frequencies. Some locations, such as WS6 and WS7, will sometimes see their greatest amplifications at wholly different azimuths.

Queen Anne's nonuniform shape makes it difficult to define its primary axis of orientation; we assume a roughly southeast axis, corresponding to its longest basal dimension. The amplifications on Queen Anne are generally smaller (ratio values of ~2) and at lower frequencies than on West Seattle (Fig. 18). Though, like West Seattle, the greatest amplifications often occur above the expected resonance frequency. The higher frequency amplifications (≥1 Hz) also tend to be quite variable from one simulation to the next, whereas the lower frequency amplifications are more persistent across simulations.

These results suggest that although topographic resonance contributes to ground shaking, there is a tendency for the response in any one scenario to stray from idealized behavior. It seems likely that modeled topographic amplification is also strongly influenced by other processes, like localized shape focusing and scattering of incoming *S* and surface waves.

As the lack of clear azimuthal amplification on Queen Anne demonstrates, deviations from archetypal morphology will complicate topographic response. Throughout the model region, we observed that the more complex a topography's morphology, or the less distinct its shape, the harder it was to identify a distinct topographic response. Similarly, the more-gentle a feature's slope, the less significant its amplification between the topography and flat simulations.

A final critical observation is that comparing records between topography and flat simulations at a given location only provides a muddled picture of how the underlying topography affects ground motions. Adding topography to a simulation will not only produce an expected topographic response, but it will also affect the overall wavefield, thus impacting the response at any individual site. Figures 13 and 14, which only compared the topography response on each feature with the flat response, inherently mixed the effects of individual topographic features with mid- and far-field scattering, often obscuring the localized topographic resonance behavior.

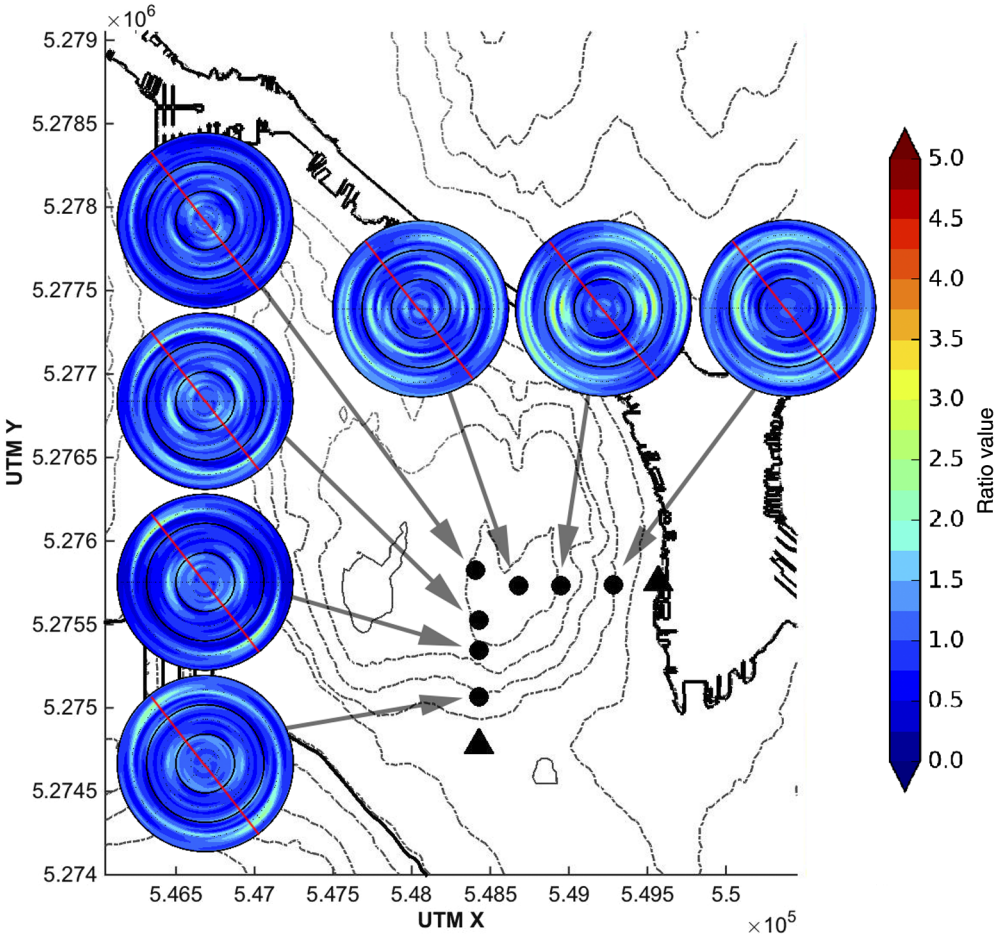

Figure 18. Polarization of horizontal spectral ratios on Queen Anne (simulation S2E). Ratios are calculated by dividing the rotated spectral response from stations at the top and slope of the cliff (black circles) by the spectral response at the bottom of the cliff (black triangles). Frequency increases outward from the center of the plot, whereas azimuths correspond to compass directions. Concentric rings mark 1 Hz intervals, with the innermost ring representing 1 Hz and the outermost ring representing 3 Hz. Colors correspond to the value of the spectral ratio at a particular frequency and azimuth. Ratio values greater than one represent amplification relative to the bottom station, whereas values less than one represent deamplification. Red lines denote the hill's approximate primary axis of orientation. The color version of this figure is available only in the electronic edition.

Therefore, the local response of topography is better quantified using our direct comparisons between the response at the top and bottom of a feature across several scenarios (Figs. 15, 16).

Variability of topographic effects

In this section, we examine the variability of simulated ground motions on account of topography from several different perspectives: the change in variability between the topography and flat simulations, changes in variability with respect to location on a topographic feature, and variability related to the kinematic rupture parameters and source location.

Variability between topography and flat simulations. To constrain the aggregate variability in response between the topography and flat simulations, we plot the percentage change in interevent PGV standard deviation (σ) versus period in Figure 19. Similar to Figure 10, the percentage change in σ at a given site was calculated by subtracting the σ in the flat simulation from the σ in the topography simulation, dividing by the σ in the flat simulation, and then multiplying the result by 100. The σ values consider the horizontal PGV results from all the nine simulations recorded on the uniform grid of stations, excluding stations situated in mountainous areas overlying bedrock.

Similar to the amplification behavior observed in Figure 10, the average change in σ is relatively low (<±10%); however, low- and mid-range periods of ground motion (≤2.0 s) experience a larger distribution in σ change than longer period ground motions. The distribution of σ change is fairly uniform for these shorter periods, with around a quarter of sites taking on σ values 25%–35% greater than in the flat simulation and another quarter seeing values 30% lower. In contrast, at 7.5 s, over 90% of the sites have σ within 30% of those predicted in the flat simulations. Additional details on the topography versus flat variability are included in the supplemental material.

Variability with location on a topographic feature. We also explicitly compare the interevent σ between the top and bottom of topographic features. In West Seattle, only 1.0 s ground motions demonstrate a uniform trend across the entire feature, with σ increasing upslope relative to the bottom at all locations (though the increase in σ is not necessarily uniform with elevation or location; Fig. 20). Otherwise, the σ at lower periods (≤0.5 s) does not appear to uniformly follow a topography-related trend. Change in σ at higher periods (≥2.0 s) is negligible.

On Queen Anne, a trend of σ increasing upslope manifests at 5.0 and 7.5 s, with σ at the top of the hill typically being 35%–40% greater than at the bottom (Fig. 21). At lower

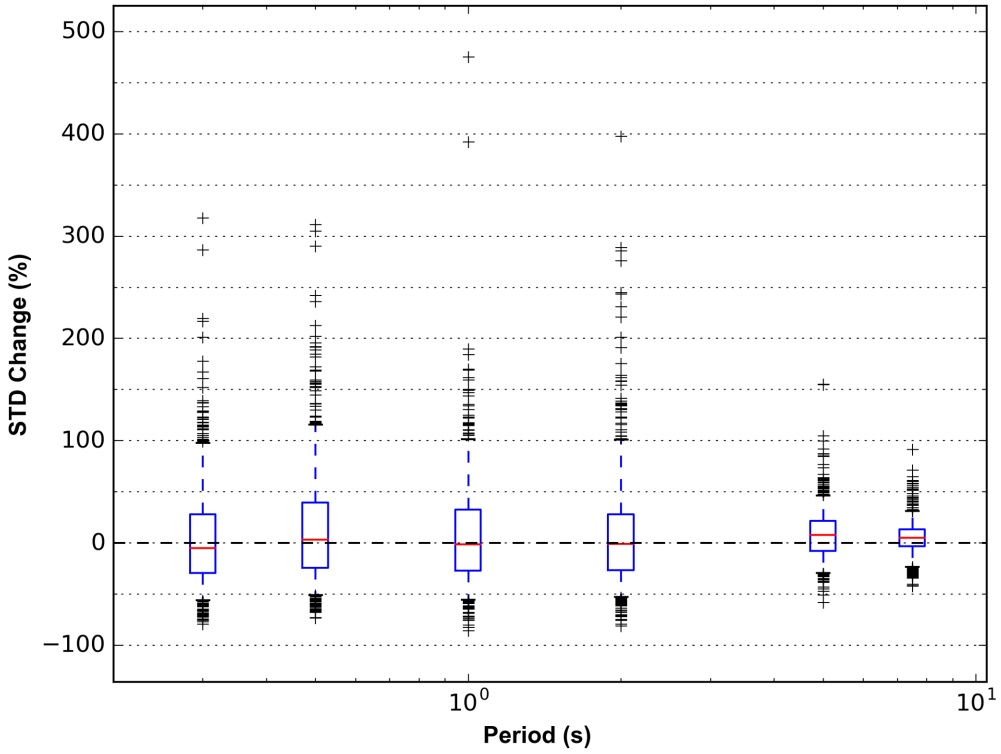

Figure 19. Distribution describing the change in standard deviation (STD) between the flat and topography simulations across all stations in the uniform grid. Location along the *x* axis represents the period of ground motion. Each box bounds 50% of observations, with the red line representing the median value of the distribution. Whiskers bound 90% of observations. Positive values represent an increase in standard deviation in the topography simulation relative to the flat simulation, whereas negative values represent a decrease in standard deviation. The color version of this figure is available only in the electronic edition.

periods, complex patterns of increased and decreased σ are present on the hill slopes.

Among all the targeted array sites, the variability in ground motions increases in a range that overlaps with the expected resonance frequency of the topographic feature. This behavior is more notable on features that also exhibited significant amplification near the topographic resonance frequency as well as on larger-scale features (e.g., Queen Anne).

Sensitivity of topographic effects to kinematic fault parameters. Ground motions in finite-fault simulations exhibit a range of sensitivities to changes in kinematic fault parameters such as hypocenter location and slip distribution (e.g., Moschetti *et al.*, 2017; Wirth *et al.*, 2017; Wirth, Frankel, *et al.*, 2018). Changing these parameters affects factors such as the distance to high-slip regions and rupture directivity effects, which in turn affect the strength, predominant azimuth, and frequency content of the incoming seismic energy at a particular location. With respect to topographic amplification, it is well established that changing the location of a seismic source has significant effects on the severity of amplification (e.g., Rodgers *et al.*, 2010; Imperatori and Mai, 2015; Restrepo *et al.*, 2016). However, it is less clear how topographic effects may change when varying kinematic fault parameters. The location of the source is not changing, but the character of the incoming seismic energy is. In this section, we explore how changing the hypocenter location and slip distribution affect simulated topographic effects.

In general, topographic amplification is highly variable from one earthquake scenario to the next. We plot polarization diagrams showing the spectral ratio between a top and bottom station in West Seattle for all the nine simulations in Figure 22, along with an averaged polarization plot derived from all the simulations. The principal amplification patterns do roughly align perpendicular to the orientation of the cliff, and ground motions are consistently amplified in discrete frequency bands between 1 and 3 Hz, as is clear from the average polarization plot. However, for any one scenario, the amount of amplification, the exact frequency at which it peaks, and its orientation may vary significantly. For instance, the plots for S1W and S3W both share a common hypocenter location. However, the S1W plot reaches a peak amplification of ~5 near 1.9 Hz at 100°, whereas the S3W plot reaches a peak amplification of ~4 near 2.8 Hz at 70°. In comparing all the simulations, sharing a common hypocenter or slip distribution does not appear to result in strongly consistent amplification behavior; further, the topographic response does not appear to be more sensitive to one parameter over the other. It should be noted, though, that lower frequency response (<1 Hz) is more consistent across all the simulations than higher frequency response.

Although a topographic feature may assume a characteristic set of behaviors that roughly manifest from one earthquake to the next, significant differences in the wavefield result in differences in response. Specifically, the variations between individual polarization plots likely represent differences in the focusing and scattering of seismic energy within or adjacent to the topographic feature, because the polarization plots only measure variations in response between a feature's top and bottom. This is supported by the insensitivity of lower frequency ground

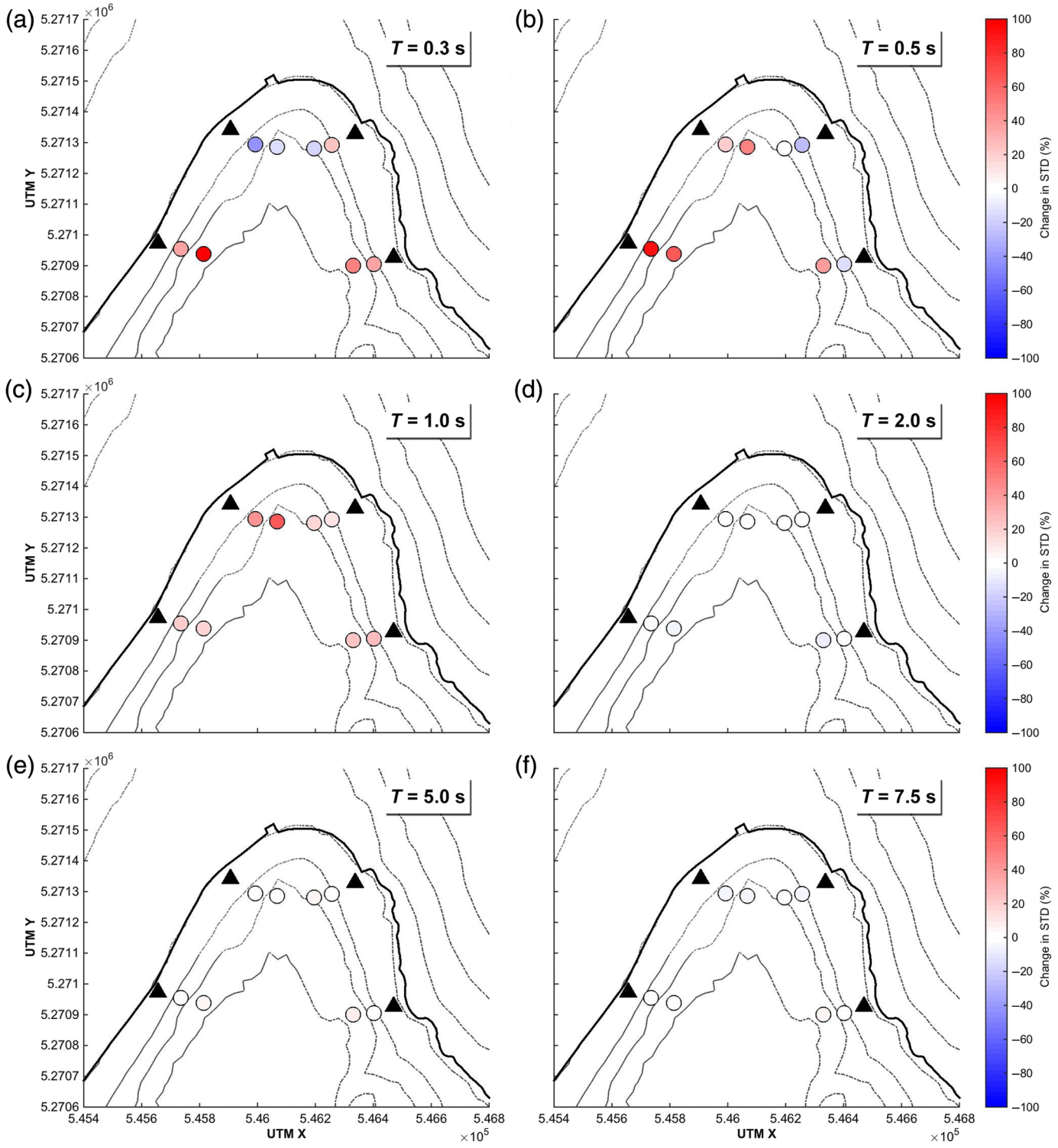

Figure 20. Change in interevent STD between the top and bottom stations on West Seattle. Periods of ground motion considered are (a) 0.3, (b) 0.5, (c) 1.0, (d) 2.0, (e) 5.0, and (f) 7.5 s. Top and slope stations are represented by colored circles, whereas the bottom stations are represented by black triangles. The color version of this figure is available only in the electronic edition.

motions to changes in slip parameters, because (as has been made clear in prior subsections) the lower frequency seismic waves are less likely to be affected by smaller scale topography.

Sensitivity of topographic effects to source location. The results for the M_w 7.0 earthquake simulations demonstrate topographic response considering only a single source extent and location. To explore the influence these factors may have

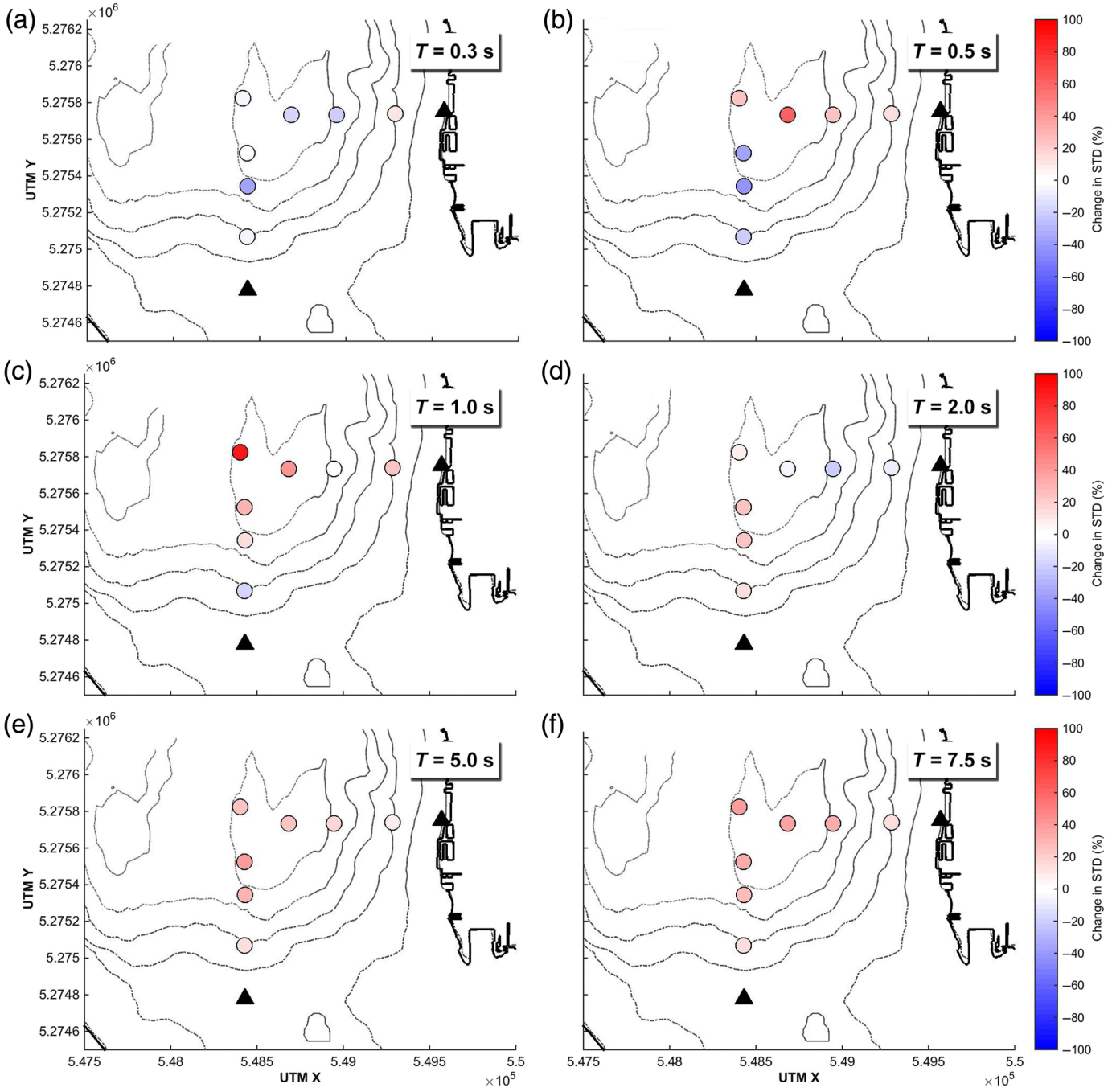

Figure 21. Change in interevent STD between the top and bottom stations on Queen Anne. Periods of ground motion considered are (a) 0.3, (b) 0.5, (c) 1.0, (d) 2.0, (e) 5.0, and (f) 7.5 s. Top and slope stations are represented by colored circles, whereas the bottom stations are represented by black triangles. The color version of this figure is available only in the electronic edition.

on topographic response, we simulate several instances of M_w 6.5 earthquakes as well. In general, the topographic amplification behaviors observed in the M_w 7.0 simulations persist in the M_w 6.5 simulations (a baseline comparison of the M_w 7.0 and 6.5 results is included in the supplemental material). However, because the source region for the M_w 6.5 earthquakes is smaller, we may change the source's location within the fault zone.

Some studies note a distinct relationship between the azimuth of an earthquake relative to the primary axis of orientation for a feature and the degree of observed amplification and/or amount of shaking effects (e.g., Meunier *et al.*, 2008; Hartzell *et al.*, 2014; Massa *et al.*, 2014). We investigate whether this behavior is present in our results by comparing spectral amplifications between M_w 6.5 events at different source locations. Each of these sources share the same slip distribution and relative hypocenter location, but the entire source is shifted either

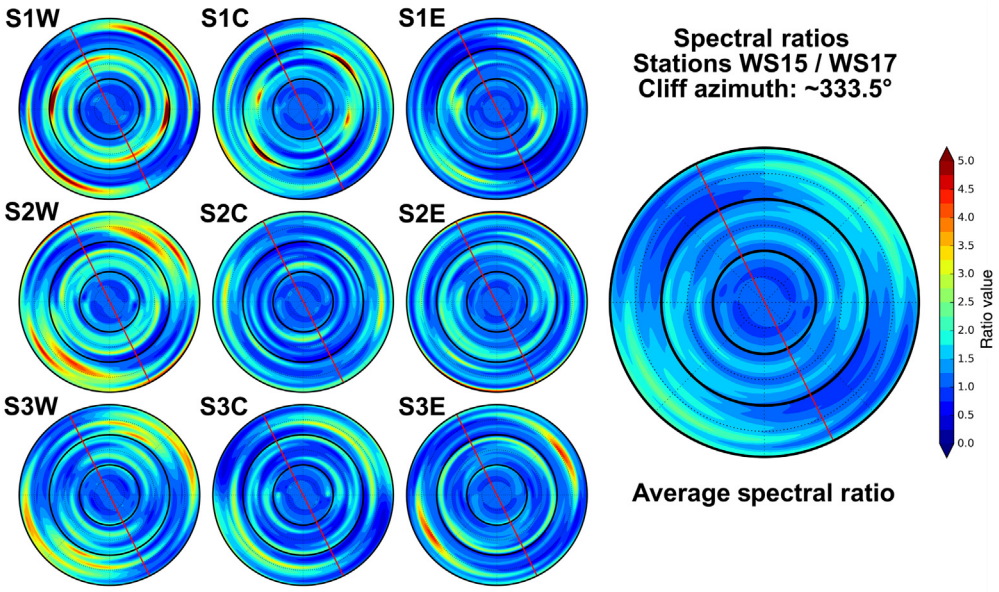

Figure 22. Polarization of horizontal spectral ratios between stations WS15 (top of cliff) and WS17 (bottom of cliff) on West Seattle. The 3 × 3 grid represents the spectral ratio between the stations for all nine M_w 7.0 simulations; columns correspond to hypocenter location (from left to right: west, central, and east hypocenter); and rows correspond to slip distribution (from top to bottom: slip distribution 1, 2, and 3). The large polar plot on the right corresponds to the geometrically averaged response of all the rose plots in the grid. The red line corresponds to the cliff's orientation. The ratio value color scale is the same across all the plots. The color version of this figure is available only in the electronic edition.

east or west along the fault zone by a ½ source length (Fig. 2). To calculate the spectral amplification, we take the horizontal velocity time series of stations at the top of targeted topographic features and convert them to the frequency domain. We then smooth the two horizontal components using a Gaussian function and combine them via a geometric average. To calculate amplification, we take the ratio of the spectrum at the top of the topographic feature to that at the foot of the topographic feature. We then find the average amplification within a 0.1 Hz window at select frequencies. In Figure 23, we plot top over bottom amplifications at station pairs in West Seattle at a range of periods relative to the source-to-site azimuth, in which each azimuth represents the direction to the centroid of moment release for each source.

In looking at the response at each of our targeted array sites, there is not a clear relationship between the source-centroid-to-site azimuth and the degree of amplification. This is to say that sources at azimuths more parallel to the primary axis of elongation do not appear to produce greater or lesser amplification relative to those more perpendicular to the axis. This observation is true for all the periods tested, including those near the analytically predicted resonance frequency. For cliff sites, there also does not seem to be a clear relationship with amplification and the direction of approach relative to the crest or foot of the cliff (e.g., amplification does not show a preference to whether a slope is facing toward or away from the source centroid).

CONCLUSIONS

We explored topographic effects on earthquake ground motions from M_w 7.0 and 6.5 earthquake scenarios on the Seattle fault in Washington. Our primary goal was to judge how adding topography may cause predicted ground motions to differ from those in typical flat finite-fault simulations and to explore the sensitivity of topographic effects to kinematic rupture parameters. On average, ground motions (PGV) at a given site in the topography model were near those predicted by the flat model, though significant amplifications (>80%) were present at some sites, particularly at shorter periods of ground motion. PGV was typically amplified at the crest of hills and cliffs and deamplified at topographic lows.

The components of the wavefield most affected by topography were the *S* and surface waves, and comparisons of PGV between crest and base stations at different periods demonstrated that amplification typically occurs near the analytically predicted topographic resonance frequency for cliffs and hills. We found that ground motions are typically the most amplified perpendicular to a feature's primary axis of elongation, but the exact direction and frequency at which maximum amplification occurs may vary somewhat from one earthquake to the next. This effect diminishes on features with more amorphous shape and gentler slopes.

Throughout the model region, the average interevent standard deviation (σ) in the topography simulations was similar to that in the flat simulations. Though for shorter periods of ground motion (≤2 s), around a quarter of sites saw an increase in σ greater than 25%, and another quarter saw a decrease greater than 30%. Changes in σ at longer periods were much less significant. In comparing the response at the top of a feature relative to its base, a systematic increase in σ was observed moving upslope, specifically at periods near the predicted topographic resonance frequency; topography-related trends were not directly apparent at other periods. The upslope increase in σ was typically the most significant for larger scale features. The reduced range of σ at longer periods relative to shorter periods mirrors the dependence of ground-motion variability on shallow velocity structure. Which is to say, longer periods of ground motion are less

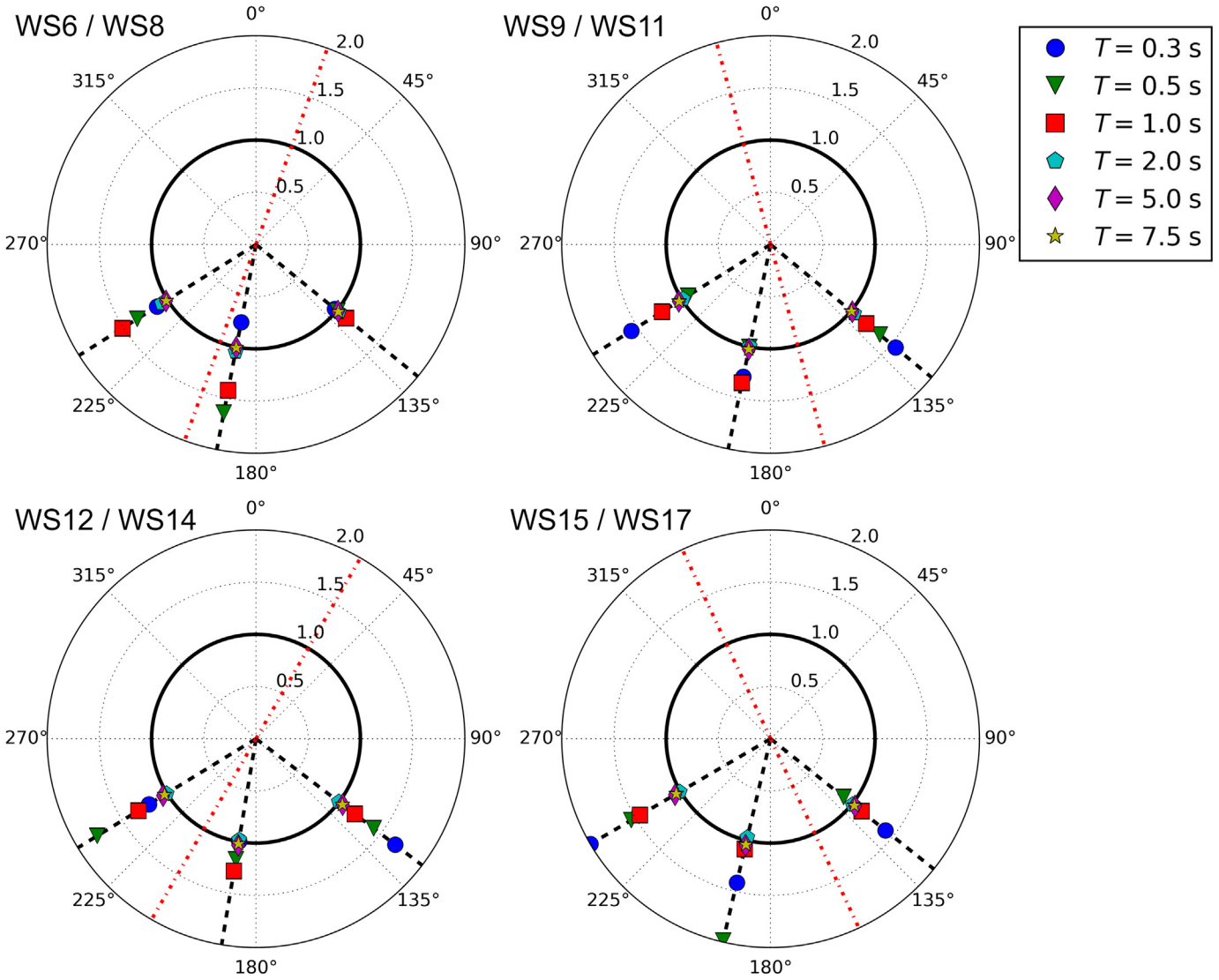

Figure 23. Amplification at different periods between the top and bottom of the cliffs in West Seattle for the different M_w 6.5 earthquake source locations. The dashed black lines correspond to the source-centroid-to-site azimuth for a particular source location. The dotted–dashed red line corresponds to the primary axis of orientation of the cliff at that location. Amplification increases from the center to the edge of the plots. Amplification corresponds to the ratio of the peak ground motion at the top of the cliff over the peak ground motion at the bottom of the cliff; values greater than one (outside the solid black circle) indicate positive amplification, whereas values less than one indicate deamplification. The color version of this figure is available only in the electronic edition.

sensitive overall to topography than shorter periods of ground motion, much in the same way longer periods of ground motion show less sensitivity to small-scale velocity heterogeneities (Moschetti *et al.*, 2017). However, this effect may be a factor of the topography present in this model region, and areas with a different topographic roughness (i.e., large mountains rather than mid-sized hills) might favor greater variability at long periods.

Results demonstrated a strong sensitivity with respect to slip distribution and hypocenter location. Amplification observations averaged across all simulations suggest that topographic resonance does typically influence ground shaking, chiefly through amplification near the resonance frequency at a predictable azimuth; however, significant variability between different rupture scenarios suggest other factors, such as localized shape focusing and scattering of *S* and surface waves, also play a significant role in the topographic response. We did not note a greater sensitivity of topographic response to one rupture parameter over another. In general, the source dependence of topographic effects is greater for higher frequencies of ground motion (>1 Hz).

We found that topographic response was generally similar between the M_w 7.0 and 6.5 earthquakes. The characteristic amplification behaviors observed in the topography versus flat models, as well as at the top and bottom of individual topographic features, persisted when the magnitude changed. In

testing different M_w 6.5 source locations, we did not see clear evidence that topographic amplification preferred source-to-size azimuths perpendicular (or parallel) to the topography's primary axis of orientation, or that amplification was dependent on whether a slope was facing toward or away from a source centroid. These results diverge from some studies of observed earthquakes, which tend to note a relationship between source-to-site azimuth and amplification (e.g., Meunier *et al.*, 2008; Hartzell *et al.*, 2014; Massa *et al.*, 2014). We suggest that this difference is in part a result of our using a finite-fault source; with the exception of Meunier *et al.* (2008), the cited studies look exclusively at records from smaller magnitude (M_w <5) earthquakes at some distance from the source. As the size of the source increases relative to the receiver, so does the breadth of azimuths from which seismic energy approaches a feature. Even for the relatively small M_w 6.5 events, the complexity of the wavefield is likely enough to confound clear azimuthal trends that manifest for lower magnitude earthquakes. Clearer azimuthal trends may present themselves in higher magnitude earthquakes for observations recorded at much larger distances (i.e., larger than what was tested in this study), in which the size of the source is small relative to the distance between the source and topographic feature. Similarly, the scale of the topography may contribute to the strength of the azimuthal response, which may help explain the disparity between the results in this study and Meunier *et al.* (2008); in that study, it was observed that earthquake-induced landslides tended to cluster on slopes facing away from the source. However, a majority of the topographic features on which distinct azimuthal variations were noted were taller (>350 m) and broader (>1.5 km) than the features looked at in this study, making them more likely to interact with coherent, long-wavelength energy.

Topographic effects in this study followed the same general patterns observed in studies of real-world ground motions, with some caveats. Topographic amplification during actual earthquakes has produced ground motions many times higher than in adjacent, flat-ground locations, as well as very strong directionality and adherence to a particular frequency range. In contrast, our results show a more muddled picture of topographic amplification—one in which topography certainly influences ground motions, but in ways that are generally subtle and only broadly predictable. Other studies have found that waveform simulations do tend to underestimate observed topographic effects, which has been attributed to simplifications in the morphology and geology of the topography (e.g., Lovati *et al.*, 2010). Although some simplifications were necessarily made in our study to accommodate the scale of the overall simulation, we did attempt to respect both the morphology and shallow geology in our model.

Instead, we suggest that the lack of significant response may be a factor of the topography within the model region. There is a gradation of response within our results that shows that features with steeper slopes do tend to have a higher amplitude topographic response—an observation that mirrors results from analytic solutions (Sánchez-Sesma, 1985, 1990). However, with respect to much of the topography surveyed in the literature (e.g., Massa *et al.*, 2014; Stolte *et al.*, 2017), even the steepest features within our model area are relatively smooth; for instance, the cliffs around West Seattle, which produced some of the more distinct topographic effects in our simulations, have a maximum slope around 30°. When considered along with strong, near-field source variability and 3D velocity structure, the individual topographic response of any one feature may be very complicated. Given that many high seismic hazard regions present similar complexities, we believe the results are reasonably representative of topographic response during finite fault rupture, particularly in nonmountainous areas. Given the degree of topographic amplification observed in this study, work should continue toward considering topography in seismic hazard studies, either through direct modeling of wave propagation or through some other novel metric.

As waveform simulations pursue ground motions at higher direct frequencies and over larger regions, we suggest a few improvements on the modeling method employed in this study. Introduction of a more realistic near-surface soil structure would likely improve the accuracy of simulations. A significant challenge for future simulations will be accurately representing ground motions in areas where soils overlie high-velocity rock, which produced large resonance patterns in our simulations. Emphasis should either be placed on high-resolution mapping of soil thicknesses in high-hazard regions or on the development of a statistical method to realistically represent soil thicknesses within velocity models. Similarly, inclusion of nonlinear soil response would help to illuminate the interplay between shallow geologic and topographic amplification effects. Extending the model area to much larger regions would make it easier to explore the contributions of directivity to topographic response during very large earthquakes. The extent of the model area in this study made it difficult to comprehensively explore the contribution of directivity (which is often the greatest in a relatively narrow azimuth range off either end of the fault) as well as topographic effects at more intermediate distances. Additional simulations with a greater variety of slip distributions and hypocenter locations would provide a stronger basis for generalizing behavior on any particular feature within the model region. Further, it would be interesting to see similar finite-fault tests run in regions with different geomorphologies. Other studies have found that the roughness of the topography in a model area has a significant control on scattering of the wavefield, which affects the spectral makeup of the wavefield at larger distances (Rodgers *et al.*, 2010; Imperatori and Mai, 2015).

DATA AND RESOURCES

The supplemental material accompanying this article contains a validation of the model against a real earthquake record, a discussion of

the selective smoothing done to the mesh and velocity model, additional details on the topography versus flat variability, and a baseline comparison of the M_w 6.5 and 7.0 results. Simulations in this article were run using Computational Infrastructure for Geodynamics code SPECFEM3D Cartesian (https://geodynamics.org/resources/specfem3dcartesian/about, last accessed April 2022). All data used in this article came from published sources listed in the references.

DECLARATION OF COMPETING INTERESTS

The authors acknowledge that there are no conflicts of interest recorded.

ACKNOWLEDGMENTS

The authors would like to thank John Vidale and Jake Dafni for helpful discussion on subjects related to this project. Thank you to Robert Graves, Morgan Moschetti, Ricardo Taborda, and two anonymous reviewers for reviewing the article and providing helpful suggestions. Simulations were run on the Stampede2 supercomputer at the Texas Advanced Computing Center at the University of Texas at Austin; funding for these resources was provided through a U.S. National Science Foundation (NSF) Extreme Science and Engineering Discovery Environment Research Allocation (Grant Number OAC-1548562). Additional support for this research was provided through the NSF's Graduate Research Fellowship Program (Grant Number DGE-1762114) and NSF Award Number EAR-1953710.

Any use of trade, firm, or product names is for descriptive purposes only and does not imply endorsement by the U. S. Government.

REFERENCES

Abrahamson, N. A., W. J. Silva, and R. Kamai (2014). Summary of the ASK14 ground motion relation for active crustal regions, *Earthq. Spectra* **30,** no. 3, 1025–1055, doi: 10.1193/070913EQS198M.

Allstadt, K., J. E. Vidale, and A. D. Frankel (2013). A scenario study of seismically induced landsliding in Seattle using broadband synthetic seismograms, *Bull. Seismol. Soc. Am.* **103,** no. 6, 2971–2992, doi: 10.1785/0120130051.

Ashford, S. A., and N. Sitar (1997). Analysis of topographic amplification of inclined shear waves in a steep coastal bluff, *Bull. Seismol. Soc. Am.* **87,** no. 3, 692–700.

Bard, P. Y. (1982). Diffracted waves and displacement field over two dimensional topographies, *Geophys. J. Int.* **71,** 731–760.

Blakely, R. J., R. E. Wells, C. S. Weaver, and S. Y. Johnson (2002). Location, structure, and seismicity of the Seattle fault zone, Washington: Evidence from aeromagnetic anomalies, geologic mapping, and seismic-reflection data, *Geol. Soc. Am. Bull.* **114,** no. 1, 169–177.

Boore, D. M. (1972). A note on the effect of simple topography on seismic SH waves, *Bull. Seismol. Soc. Am.* **62,** no. 1, 275–284.

Boore, D. M. (2010). Orientation-independent, nongeometric-mean measures of seismic intensity from two horizontal components of motion, *Bull. Seismol. Soc. Am.* **100,** no. 4, 1830–1835, doi: 10.1785/0120090400.

Boore, D. M., J. P. Stewart, E. Seyhan, and G. M. Atkinson (2014). NGA-West2 equations for predicting PGA, PGV, and 5% damped PSA for shallow crustal earthquakes, *Earthq. Spectra* **30,** no. 3, 1057–1085, doi: 10.1193/070113EQS184M.

Bouchon, M., C. A. Schultz, and M. N. Toksöz (1996). Effect of three-dimensional topography on seismic motion, *J. Geophys. Res.* **101,** no. B3, 5835–5846.

Brune, J. N. (1970). Tectonic stress and the spectra of seismic shear waves from earthquakes, *J. Geophys. Res.* **75,** no. 26, 4997–5009, doi: 10.1029/JB075i026p04997.

Campbell, K. W., and Y. Bozorgnia (2014). NGA-West2 ground motion model for the average horizontal components of PGA, PGV, and 5% damped linear acceleration response spectra, *Earthq. Spectra* **30,** no. 3, 1087–1114, doi: 10.1193/062913EQS175M.

Celebi, M. (1987). Topographical and geological amplifications determined from strong-motion and aftershock records of the 3 March 1985 Chile earthquake, *Bull. Seismol. Soc. Am.* **77,** no. 4, 1147–1167.

Chiou, B. S. J., and R. R. Youngs (2014). Update of the Chiou and Youngs NGA model for the average horizontal component of peak ground motion and response spectra, *Earthq. Spectra* **30,** no. 3, 1117–1153, doi: 10.1193/072813EQS219M.

Davis, L. L., and L. R. West (1973). Observed effects of topography on ground motion, *Bull. Seismol. Soc. Am.* **63,** no. 1, 747–763.

Dreger, D. S., G. C. Beroza, S. M. Day, C. A. Goulet, T. H. Jordan, P. A. Spudich, and J. P. Stewart (2015). Validation of the SCEC Broadband Platform V14.3 simulation methods using pseudospectral acceleration data, *Bull. Seismol. Soc. Am.* **86,** no. 1, 39–47, doi: 10.1785/0220140118.

Fichtner, A. (2011). The spectral-element method, in *Full Seismic Waveform Modelling and Inversion*,K. Hutter (Editor), Springer, New York, New York, 182–210.

Finlayson, D. P. (2005). *Combined Bathymetry and Topography of the Puget Lowland*, Washington State, University of Washington, available at https://www.ocean.washington.edu/data/pugetsound/psdem2005.html (last accessed September 2020).

Frankel, A. D., D. L. Carver, and R. A. Williams (2002). Nonlinear and linear site response and basin effects in Seattle for the M 6.8 Nisqually, Washington, earthquake, *Bull. Seismol. Soc. Am.* **92,** no. 6, 2090–2109, doi: 10.1785/0120010254.

Frankel, A. D., W. J. Stephenson, and D. L. Carver (2009). Sedimentary basin effects in Seattle, Washington : Ground-motion observations and 3D simulations, *Bull. Seismol. Soc. Am.* **99,** no. 3, 1579–1611, doi: 10.1785/0120080203.

Frankel, A. D., W. J. Stephenson, D. L. Carver, R. A. Williams, J. K. Odum, and S. Rhea (2007). Seismic hazard maps for Seattle, Washington, incorporating 3D sedimentary basin effects, nonlinear site response, and rupture directivity, *U.S. Geol. Surv Open-File Rept. 2007-1175*, 77 pp.

Frankel, A. D., P. Thorne, and A. Rohay (2014). Three-dimensional ground-motion simulations of earthquakes for the Hanford Area, Washington, *U.S. Geol. Surv. Open-File Rept. 2013-1289*, 48 pp.

Frankel, A. D., E. A. Wirth, N. Marafi, J. Vidale, and W. J. Stephenson (2018). Broadband synthetic seismograms for magnitude 9 earthquakes on the Cascadia megathrust based on 3D simulations and stochastic synthetics, Part 1: Methodology and overall results, *Bull. Seismol. Soc. Am.* **108,** no. 5, 2347–2369, doi: 10.1785/0120180034.

Geli, L., P.-Y. Bard, and B. Jullien (1988). The effect of topography on earthquake ground motion: A review and new results, *Bull. Seismol. Soc. Am.* **78,** no. 1, 42–63.

Hartzell, S., S. Harmsen, and A. D. Frankel (2010). Effects of 3D random correlated velocity perturbations on predicted ground motions, *Bull. Seismol. Soc. Am.* **100,** no. 4, 1415–1426, doi: 10.1785/0120090060.

Hartzell, S., M. Meremonte, L. Ramírez-Guzmán, and D. McNamara (2014). Ground motion in the presence of complex topography: Earthquake and ambient noise sources, *Bull. Seismol. Soc. Am.* **104,** no. 1, 451–466, doi: 10.1785/0120130088.

Hartzell, S. H., D. L. Carver, and K. W. King (1994). Initial investigation of site and topographic effects at Robinwood Ridge, California, *Bull. Seismol. Soc. Am.* **84,** no. 5, 1336–1349.

Hough, S. E., J. R. Altidor, D. Anglade, D. Given, M. G. Janvier, J. Z. Maharrey, M. Meremonte, B. S. L. Mildor, C. Prepetit, and A. Yong (2010). Localized damage caused by topographic amplification during the 2010 M7.0 Haiti earthquake, *Nature Geosci.* **3,** no. 11, 778–782, doi: 10.1038/ngeo988.

Imperatori, W., and P. M. Mai (2015). The role of topography and lateral velocity heterogeneities on near-source scattering and ground-motion variability, *Geophys. J. Int.* **202,** no. 3, 2163–2181, doi: 10.1093/gji/ggv281.

Komatitsch, D., Q. Liu, J. Tromp, P. Süss, C. Stidham, and J. H. Shaw (2004). Simulations of ground motion in the Los Angeles basin based upon the spectral-element method, *Bull. Seismol. Soc. Am.* **94,** no. 1, 187–206, doi: 10.1785/0120030077.

Lee, S. J., Y. C. Chan, D. Komatitsch, B. S. Huang, and B. S. Tromp (2009). Effects of realistic surface topography on seismic ground motion in the Yangminshan region of Taiwan based upon the spectral-element method and LiDAR DTM, *Bull. Seismol. Soc. Am.* **99,** no. 2A, 681–693, doi: 10.1785/0120080264.

Lee, S. J., H. W. Chen, Q. Liu, D. Komatitsch, B. S. Huang, and J. Tromp (2008). Three-dimensional simulations of seismic-wave propagation in the Taipe basin with realistic topography based upon the spectral-element method, *Bull. Seismol. Soc. Am.* **98,** no. 1, 253–264, doi: 10.1785/0120070033.

Lovati, S., M. K. H. Bakavoli, M. Massa, G. Ferretti, F. Pacor, R. Paolucci, E. Haghshenas, and M. Kamalian (2010). Estimation of topographical effects at Narni ridge (Central Italy): comparisons between experimental results and numerical modelling, *Bull. Earthq. Eng.* **9,** 1987–2005, doi: 10.1007/s10518-011-9315-x.

Mai, P. M., and G. C. Beroza (2002). A spatial random field model to characterize complexity in earthquake slip, *J. Geophys. Res.* **107,** no. B11, ESE 10-1–ESE 10-21, doi: 10.1029/2001jb000588.

Martel, L., M. Munasinghe, and G. W. Farnell (1977). Transmission and reflection of Rayleigh wave through a step, *Bull. Seismol. Soc. Am.* **67,** no. 5, 1277–1290.

Massa, M., S. Barani, and S. Lovati (2014). Overview of topographic effects based on experimental observations: Meaning, causes and possible interpretations, *Geophys. J. Int.* **197,** 1537–1550, doi: 10.1093/gji/ggt341.

Meunier, P., N. Hovius, and J. A. Haines (2008). Topographic site effects and the location of earthquake induced lanslides, *Earth Planet. Sci. Lett.* **275,** nos. 3/4, 221–232, doi: 10.1016/j.epsl.2008.07.020.

Moschetti, M. P., S. Hartzell, L. Ramírez-Guzmán, A. D. Frankel, S. J. Angster, and W. J. Stephenson (2017). 3D ground-motion simulations of Mw 7 earthquakes on the Salt Lake City segment of the Wasatch Fault Zone: Variability of long-period (T ≥ 1 s) ground motions and sensitivity to kinematic rupture parameters, *Bull. Seismol. Soc. Am.* **107,** no. 4, 1704–1723, doi: 10.1785/0120160307.

Paolucci, R. (2002). Amplification of earthquake ground motion by steep topographic irregularities, *Earthq. Eng. Struct. Dynam.* **31,** no. 10, 1831–1853, doi: 10.1002/eqe.192.

Pedersen, H., B. Le Brun, D. Hatzfeld, M. Campillo, and P. Y. Bard (1994). Ground-motion amplitude across ridges, *Bull. Seismol. Soc. Am.* **84,** no. 6, 1786–1800.

Pischiutta, M., G. Cultrera, A. Caserta, L. Luzi, and A. Rovelli (2010). Topographic effects on the hill of Nocera Umbra, central Italy, *Geophys. J. Int.* **182,** no. 2, 977–987, doi: 10.1111/j.1365-246X.2010.04654.x.

Pitarka, A., A. Akinci, P. GoriDe, and M. Buttinelli (2021). Deterministic 3D ground-motion simulations (0-5 Hz) and surface topography effects of the 30 October 2016 Mw 6.5 Norcia, Italy, earthquake, *Bull. Seismol. Soc. Am.* **112,** 262–286, doi: 10.1785/0120210133.

Ramachandran, K., R. D. Hyndman, and T. M. Brocher (2006). Regional P wave velocity structure of the Northern Cascadia Subduction Zone, *J. Geophys. Res.* **111,** no. 12, 1–15, doi: 10.1029/2005JB004108.

Rekoske, J. M., M. P. Moschetti, and E. M. Thompson (2021). Basin and site effects in the U.S. Pacific Northwest from small-magnitude earthquakes, *Bull. Seismol. Soc. Am.* **112,** 438–456, doi: 10.1785/0120210029.

Restrepo, D., J. Bielak, R. Serrano, J. Gómez, and J. Jaramillo (2016). Effects of realistic topography on the ground motion of the Colombian Andes—A case study at the Aburra Valley, Antioquia, *Geophys. J. Int.* **204,** no. 3, 1801–1816, doi: 10.1093/gji/ggv556.

Rodgers, A. J., N. A. Petersson, and B. Sjogreen (2010). Simulation of topographic effects on seismic waves from shallow explosions near the North Korean nuclear test site with emphasis on shear wave generation, *J. Geophys. Res.* **115,** no. B11, doi: 10.1029/2010JB007707.

Sánchez-Sesma, F. (1985). Diffraction of elastic Sh waves by wedges, *Bull. Seismol. Soc. Am.* **75,** no. 5, 1435–1446, doi: 10.2138/am-2001-2-311.

Sánchez-Sesma, F. J. (1990). Elementary solutions for response of a wedge-shaped medium to incident SH and SV waves, *Bull. Seismol. Soc. Am.* **80,** no. 3, 737–742.

Sánchez-Sesma, F. J., I. Herrera, and J. Avilés (1982). A boundary method for elastic wave diffraction: Application to scattering of SH waves by surface irregularities, *Bull. Seismol. Soc. Am.* **72,** no. 2, 473–490.

Somerville, P., K. Irikura, R. Graves, S. Sawada, D. Wald, N. Abrahamson, Y. Iwasaki, T. Kagawa, N. Smith, and A. Kowada (1999). Characterizing crustal earthquake slip models for the prediction of strong ground motion, *Seismol. Res. Lett.* **70,** no. 1, 59–80, doi: 10.1785/gssrl.70.1.59.

Spudich, P., M. Hellweg, and W. H. K. Lee (1996). Directional topographic site response at Tarzana observed in aftershocks of the 1994 Northridge, California, earthquake: Implications for mainshock motions, *Bull. Seismol. Soc. Am.* **86,** no. 1B, S193–S208.

Stephenson, W. J., N. G. Reitman, and S. J. Angster (2017). P- and S-wave velocity models incorporating the Cascadia subduction zone

for 3D earthquake ground motion simulations—Update for Open-File Report 2007–1348, *U.S. Geol. Surv. Open-File Rept. 2017-1152*, doi: 10.3133/ofr20171152.

Stolte, A. C., B. R. Cox, and R. C. Lee (2017). An experimental topographic amplification study at Los Alamos national laboratory using ambient vibrations, *Bull. Seismol. Soc. Am.* **107,** no. 3, 1386–1401, doi: 10.1785/0120160269.

Thompson, M., E. A. Wirth, A. D. Frankel, J. R. Hartog, and J. E. Vidale (2020). Basin amplification effects in the Puget Lowland, Washington, from strong-motion recordings and 3D simulations, *Bull. Seismol. Soc. Am.* **110,** no. 2, 534–555, doi: 10.1785/0120190211.

U.S. Geological Survey (USGS) (2017). 1/3rd arc-second Digital Elevation Models (DEMs), available at https://www.usgs.gov/core-science-systems/ngp/3dep (last accessed September 2020).

Wells, D. L., and K. J. Coppersmith (1994). New empirical relationships among magnitude, rupture length, rupture width, rupture area, and surface displacement, *Bull. Seismol. Soc. Am.* **84,** no. 4, 974–1002.

Wirth, E. A., S. W. Chang, and A. D. Frankel (2018). 2018 report on incorporating sedimentary basin response into the design of tall buildings in Seattle, Washington, *U.S. Geol. Surv. Open-File Rept. 2018-1149*, doi: 10.3133/ofr20181149.

Wirth, E. A., A. D. Frankel, N. Marafi, J. E. Vidale, and W. J. Stephenson (2018). Broadband synthetic seismograms for magnitude 9 earthquakes on the Cascadia megathrust based on 3D simulations and stochastic synthetics, Part 2: Rupture parameters and variability, *Bull. Seismol. Soc. Am.* **108,** no. 5, 2370–2388, doi: 10.1785/0120180029.

Wirth, E. A., A. D. Frankel, and J. E. Vidale (2017). Evaluating a kinematic method for generating broadband ground motions for great subduction zone earthquakes : Application to the 2003 Mw 8.3 Tokachi-Oki earthquake, *Bull. Seismol. Soc. Am.* **107,** no. 4, 1737–1753, doi: 10.1785/0120170065.

Manuscript received 12 October 2021
Published online 3 May 2022